



Deposited via The University of Leeds.

White Rose Research Online URL for this paper:

<https://eprints.whiterose.ac.uk/id/eprint/133712/>

Version: Accepted Version

Article:

Bell, D, Kane, IA, Ponten, ASM et al. (2018) Spatial variability in depositional reservoir quality of deep-water channel-fill and lobe deposits. *Marine and Petroleum Geology*, 98. pp. 97-115. ISSN: 0264-8172

<https://doi.org/10.1016/j.marpetgeo.2018.07.023>

© 2018 Elsevier Ltd. Licensed under the Creative Commons Attribution-NonCommercial-NoDerivatives 4.0 International License (<http://creativecommons.org/licenses/by-nc-nd/4.0/>).

Reuse

This article is distributed under the terms of the Creative Commons Attribution-NonCommercial-NoDerivs (CC BY-NC-ND) licence. This licence only allows you to download this work and share it with others as long as you credit the authors, but you can't change the article in any way or use it commercially. More information and the full terms of the licence here: <https://creativecommons.org/licenses/>

Takedown

If you consider content in White Rose Research Online to be in breach of UK law, please notify us by emailing eprints@whiterose.ac.uk including the URL of the record and the reason for the withdrawal request.

1 **Spatial variability in depositional reservoir quality of deep-water channel-fill and lobe**
2 **deposits**

3 Daniel Bell^{1*}, Ian A. Kane¹, Anna S. M. Pontén², Stephen S. Flint³, David M. Hodgson⁴ and
4 Bonita J. Barrett⁴

5

6 ¹ SedRESQ, School of Earth and Environmental Sciences, University of Manchester,
7 Manchester, M13 9PL, U.K.

8 ² Equinor ASA, Research Center Rotvoll, NO-7005 Trondheim, Norway

9 ³ Stratigraphy Group, School of Earth and Environmental Sciences, University of Manchester,
10 Manchester, M13 9PL, U.K.

11 ⁴ Stratigraphy Group, School of Earth and Environment, University of Leeds, Leeds, LS2 9JT,
12 U.K

13 Email: daniel.bell-2@manchester.ac.uk

14 Keywords: deep-water sedimentology, reservoir quality, turbidites, submarine channel, submarine
15 lobe, Pyrenees, process sedimentology, sedimentary petrology

16 **Abstract**

17 Initial porosity and permeability in deep-water systems is controlled by primary sedimentary
18 texture and mineralogy. Therefore, understanding the sedimentary processes that control changes
19 in primary texture is critical for improved reservoir quality predictions. A well-constrained,
20 exhumed submarine lobe in the Jaca Basin, and a submarine channel-fill element in the Aínsa
21 Basin, northern Spain, were studied to characterize the depositional reservoir quality in axial to

22 marginal/fringe positions. Construction of architectural panels and strategic sampling enabled
23 analysis of the spatial changes in textural properties, and their relationship to reservoir quality
24 distribution. Samples were analysed in thin-section to establish how depositional processes
25 inferred from outcrop observations affect textural properties. Results show that high-density
26 turbidites are concentrated in lobe- and channel-axis positions and exhibit good depositional
27 reservoir quality. Lobe off-axis deposits contain high- and low-density turbidites and have
28 moderate depositional reservoir quality. Conversely, low-density turbidites dominate lobe fringe
29 and channel-margin positions and have relatively poor depositional reservoir quality. There is a
30 sharp decrease in depositional reservoir quality between the lobe off-axis and lobe fringe due to:
31 1) an abrupt increase in matrix content; 2) an abrupt decrease in sandstone amalgamation; and 3)
32 a decrease in grain-size. There is an abrupt increase in depositional reservoir quality from channel
33 margin to channel axis corresponding to: 1) an increase in total sandstone thickness and
34 amalgamation; 2) an increase in grain-size, 3) a decrease in matrix content. Rates of change of key
35 properties are up to two orders of magnitude greater between channel-fill sub-environments
36 compared to lobe sub-environments. Spatial variability in properties of discrete architectural
37 elements, and rates of changes, provides input to reservoir models during exploration, appraisal,
38 and development phases of hydrocarbon fields.

39 **1.1 Introduction**

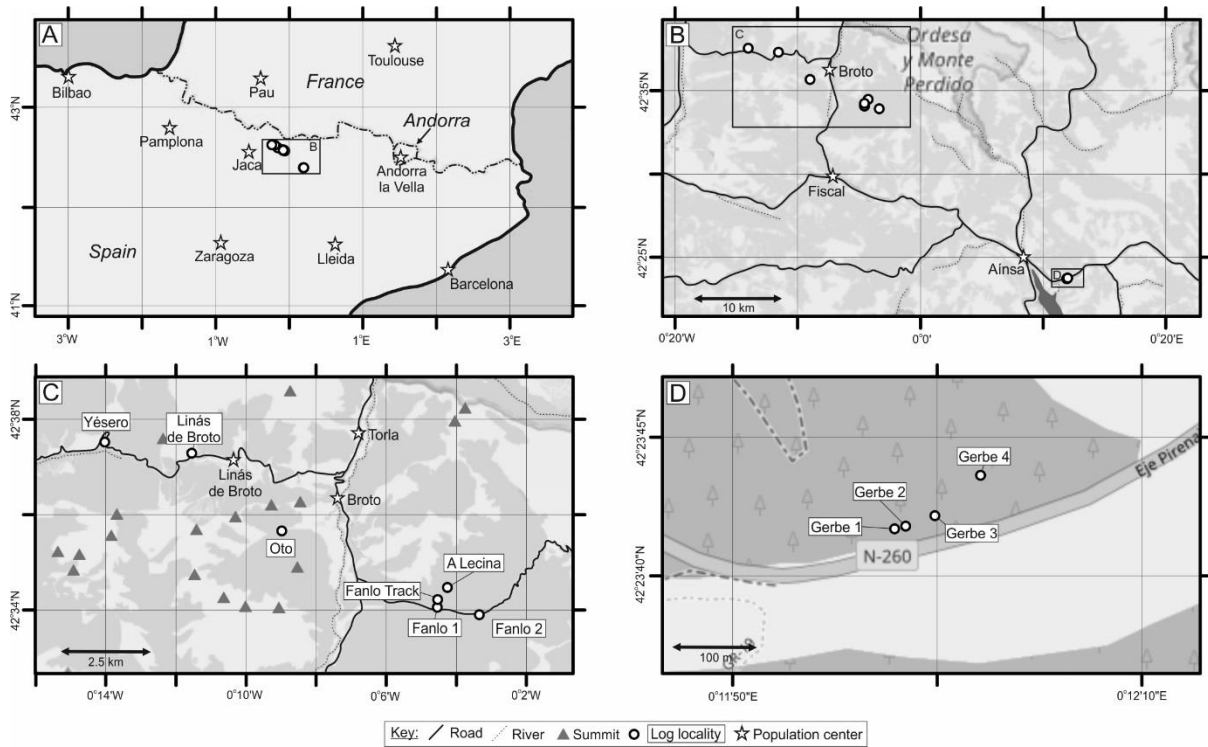
40 Submarine fans represent large volumes of terrigenous sediment transported from the
41 continental shelf to the slope and basin floor (e.g. Emmel and Curray, 1983; Piper et al., 1999;
42 Talling et al., 2007; Pr elat et al., 2010; Clare et al., 2014). Modern deep-marine systems are
43 repositories for anthropogenically derived sediment and pollutants, and organic matter (e.g. Galy
44 et al., 2007; Saller et al., 2008; Hodgson, 2009; Gwiazda et al., 2015), and buried systems form
45 reservoirs for groundwater and hydrocarbons, as well as economic accumulations of minerals (e.g.
46 Pettingill, 1998; Ruffell et al., 1998; Weimer et al., 2000; McKie et al., 2015). Consequently,

47 understanding the distribution of depositional facies and their porosity and permeability is key to
48 understanding the distribution and stability of subsurface fluids and minerals (Lien et al., 2006;
49 Porten et al., 2016; Southern et al., 2017).

50 The porosity of unconsolidated sediments is controlled by the grain-size, sorting and
51 packing of grains (Fraser, 1935; Beard and Weyl, 1973; Hirst et al., 2002; Lien et al., 2006; Njoku
52 and Pirmez, 2011; Porten et al., 2016), whereas detrital clay content, clay mineralogy, and clay
53 distribution have a strong control on permeability (e.g. Wilson, 1992; Hirst et al., 2002; Lien et al.,
54 2006; Ajdukiewicz et al., 2010; Dowey et al., 2012; Porten et al., 2016). These relationships are
55 demonstrated in terrestrial and shallow-marine deposits (e.g. Pryor, 1973; Haile et al., 2017).
56 However, the general inaccessibility of modern deep-water systems means the primary distribution
57 of their textural characteristics is less-well understood.

58 Controls on reservoir quality operate on a range of scales. At the largest-scale, sandstone
59 reservoir quality is determined by the volume of the deposit and connectivity, as elements include
60 both sand and non-sand reservoir (e.g. Kerr and Jirik, 1990; Hardage et al., 1996; Afifi, 2005; Jolley
61 et al., 2010; Kilhams et al., 2015; Lan et al., 2016). Within the sandstone portion of the reservoir,
62 ‘quality’ is predominantly determined by grain-scale porosity and permeability (e.g. Fraser, 1935;
63 Marzano, 1988; Ramm and Bjørlykke, 1994; Ehrenberg, 1997; Worden et al., 2000; Marchand et
64 al., 2015; Porten et al., 2016), which is modified by eodiagenetic and mesodiagenetic processes (e.g.
65 Ehrenberg, 1989; Pittman and Larese, 1991; Ramm and Bjørlykke, 1994; Ehrenberg, 1997; Worden
66 et al., 2000). It is recognized that the primary texture of depositional facies in deep-water
67 sandstones can also maintain a strong control even after diagenesis (Hirst et al., 2002; Lien et al.,
68 2006; Njoku and Pirmez, 2011; Kilhams et al., 2012; Marchand et al., 2015; Porten et al., 2016).
69 “Depositional reservoir quality” is the initial reservoir potential of a sedimentary accumulation
70 prior to post-depositional modification (Porten et al., 2016). The type of flow that generates a
71 deposit has a strong influence on its texture (Hirst et al., 2002; Lien et al., 2006; Njoku and Pirmez,

72 2011; Kilhams et al., 2012; Porten et al., 2016; Kane et al., 2017). Therefore, the primary texture
 73 of deposits from discrete flow-types can also maintain a strong control during all stages of
 74 diagenesis (Hirst et al., 2002; Lien et al., 2006; Njoku and Pirmez, 2011; Kilhams et al., 2012;
 75 Marchand et al., 2015; Porten et al., 2016).



77 Figure 1: A) Location of study area in Spain; B) Regional locality map showing the two studied areas; C)
 78 Localities of the Gerbe channel-fill outcrops; D) Localities of Upper Broto, Lobe 1 outcrops. Image
 79 sources: Esri, DeLorme, HERE, MapmyIndia, OpenStreetMap contributors.

80 Deep-water systems consist of depositional elements, which are hierarchically organized
 81 (e.g. Mutti and Ricci-Lucchi, 1972; Mutti, 1985; Mutti and Normark, 1987; Clark and Pickering,
 82 1996; Sprague et al., 2002; Deptuck et al., 2008; Prélat et al., 2009; Di Celma et al., 2011), the
 83 organization of which controls the overall size and connectivity of a reservoir. Architectural
 84 elements are determined by their size, architecture, bounding surfaces, and relationship to other
 85 architectural elements (e.g. Miall, 1985; Mutti and Normark, 1987; Clark and Pickering, 1996;
 86 Sprague et al., 2002; Prélat et al., 2009). Individual depositional facies have variable grain-scale

87 textures, and therefore the spatial arrangement of these depositional facies within an architectural
88 element will determine reservoir potential distribution at that hierarchical level. The stacking of
89 architectural elements and their inherited grain-scale texture allows prediction of reservoir quality
90 at higher levels in the architectural hierarchy. Therefore, understanding facies distribution and
91 grain-scale character is critical to improved prediction of reservoir distribution. Previous
92 publications related to the integration of architectural- and grain-scale observations typically
93 consider broad proximal-to-distal trends, or consider facies variability with limited spatial control
94 (Hirst et al., 2002; Lien et al., 2006; Njoku and Pirmez, 2011; Kilhams et al., 2012; Marchand et al.,
95 2015; Porten et al., 2016). Geochemical and mineralogical variations have been recognized within
96 a deep-water channel complex and attributed to the primary texture (Aehnelt et al., 2013).
97 However, no published work has attempted to constrain the depositional reservoir quality within
98 a single architectural element. To assess this issue the following research questions will be
99 addressed: 1) How can an architectural element be characterized at grain-scale? 2) How does
100 reservoir potential vary spatially within an individual architectural element? 3) How do sediment
101 gravity flow processes influence depositional reservoir quality and its distribution?

102 **2.1 Geological setting**

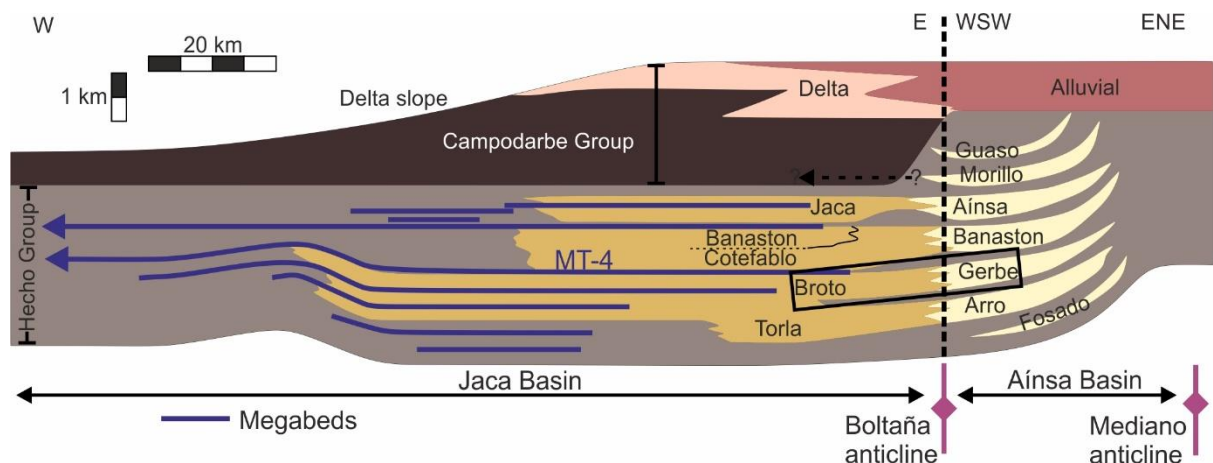
103 During the Early Eocene the Aínsa-Jaca Basin developed as an east-west trending,
104 southward migrating foredeep (Puigdefàbregas et al., 1975; Mutti, 1984; Labaume et al., 1985;
105 Mutti, 1985; Mutti et al., 1988; Muñoz, 1992; Teixell and García-Sansegundo, 1995). The deep-
106 water deposits form the Hecho Group (Fig. 2; Mutti, 1985). The Aínsa Basin fill predominantly
107 consists of submarine slope channel systems and mass-transport deposits, separated by marlstones
108 (e.g. Mutti, 1977; Clark et al., 1992; Mutti, 1992; Clark and Pickering, 1996; Remacha et al., 2003;
109 Pickering and Corregidor, 2005; Moody et al., 2012; Dakin et al., 2013; Bayliss and Pickering, 2015).
110 The Gerbe System (Fig. 2) is interpreted as a canyon to lower-slope channel system (Mutti, 1992;

111 Clark and Pickering, 1996), and consists of: 1) a lower unit that comprizes conglomerate lags,
 112 which is interpreted as sediment bypass-dominated; and 2) an upper unit that comprizes fining-
 113 upward channel-fill elements and records the aggradation and shutdown of the channel system
 114 (Mutti, 1992). This study analyzes one channel-fill element from the upper unit.

115 The Jaca Basin succession, which is separated from the exposed part of the Aínsa Basin by
 116 the Boltaña Anticline, is interpreted as a series of submarine fans, consisting of lobes and basin-
 117 plain deposits (Fig. 2; Mutti, 1977; Mutti, 1992; Remacha et al., 2005; Bell et al., *in press*). The
 118 stratigraphy of the basin-fill is constrained by nine regionally mapped ‘megabeds’ (Rupke, 1976;
 119 Labaume et al., 1987; Rosell and Wiezorek, 1989; Payros et al., 1999).

120

121



122

123 Figure 2: Stratigraphy and geological setting of the Aínsa-Jaca Basin fill. Regional depositional dip is from
 124 right to left, with tentative correlation across the Boltaña anticline following Das Gupta and Pickering
 125 (2008).

126 The lobe component of this study focuses on the Upper Broto System, immediately
 127 underlying the MT-4 megabed (see also: Mutti, 1992). The Upper Broto is interpreted as proximal
 128 lobes (Mutti, 1992; Bell et al., *in press*), with distal hybrid bed dominated packages where

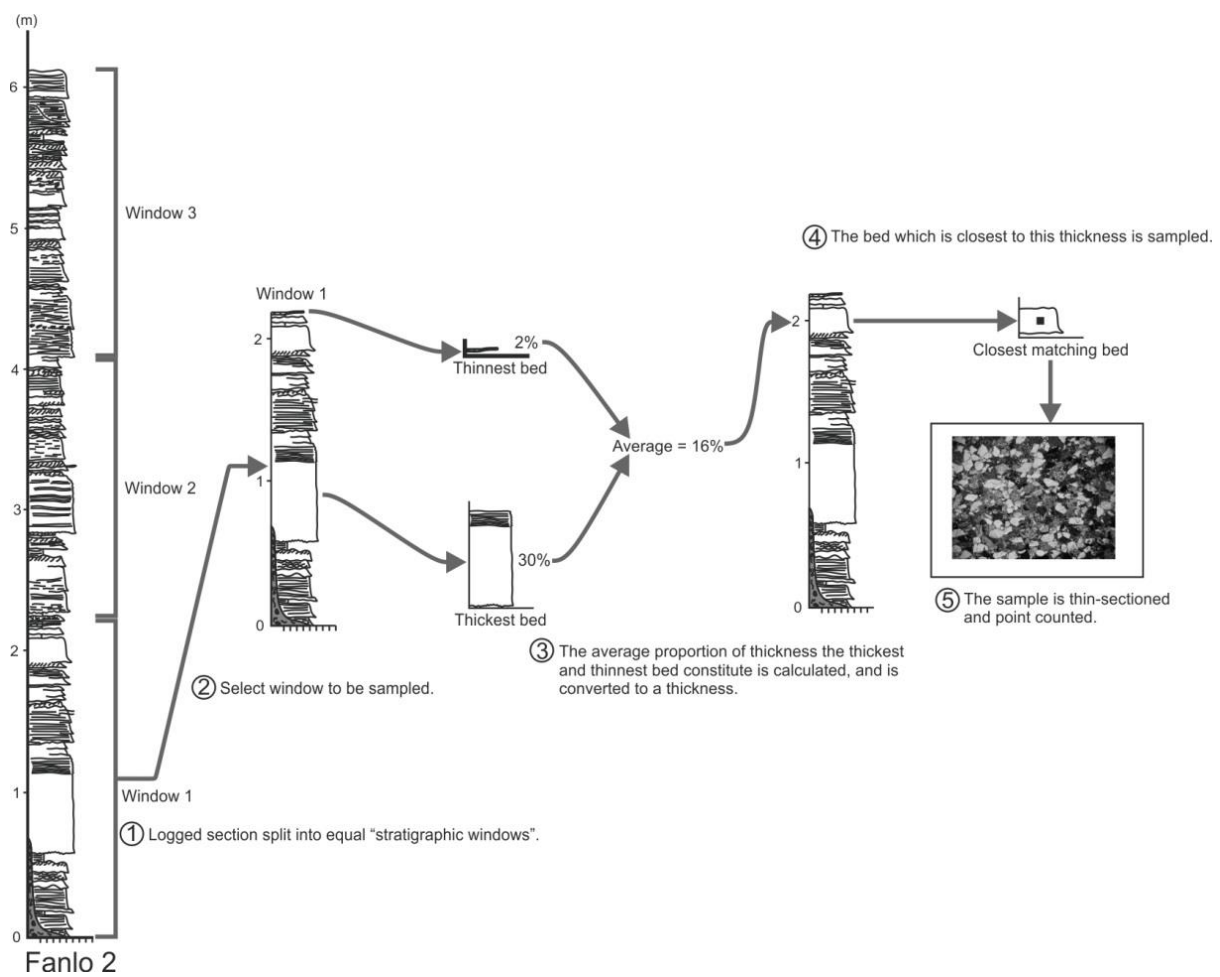
129 depositional architecture is interpreted to have been influenced by topography (Remacha and
130 Fernández, 2003; Remacha et al., 2005 Bell et al. *in press*);).

131 **3.1 Methods**

132 Different stratigraphic correlations between the Aínsa and Jaca Basins have been proposed
133 (Mutti, 1984; Mutti, 1985; Mutti, 1992; Remacha et al., 2003; Das Gupta and Pickering, 2008; Caja
134 et al., 2010; Clark et al., 2017). Following Das Gupta and Pickering (2008), the Gerbe (Aínsa) and
135 Broto (Jaca) Systems are considered as broadly equivalent and are studied here. Whilst uncertainty
136 remains with this correlation, the two systems form part of the genetically related wider basin-fill,
137 have the same burial history, and, for the puposes of this study, are comparable. Furthermore,
138 linked channel-fills and lobes may accumulate diachronously (e.g. Hodgson et al., 2016), and
139 challenges in correlating individual channel-fills with individual lobes at outcrop mean that
140 sampling the exact time-equivalent stratigraphy may not be possible. One channel-fill element and
141 one lobe were selected from the outcrops to be studied in detail. Detailed sedimentary logs and
142 thin-section analysis were used to investigate spatial changes in architecture, facies and grain-scale
143 texture within the channel-fill and lobe.

144 In the subsurface, reservoir intervals are typically sampled by core plugging at regular intervals,
145 and are biased towards sandstone. These sampling protocols are not designed to capture variability
146 at the architectural element scale. An alternative approach is to sample beds that conform to the
147 mean average bed thickness in an architectural element. However, this would preferentially select
148 thinner beds, which are more common than medium- or thick-bedded sandstone, but typically
149 account for a smaller proportion of the overall sandstone content. Therefore, to characterize an
150 architectural element at grain-scale a repeatable ‘stratigraphic sampling’ method was developed to
151 sample an ‘average’ bed characteristic of the sampled succession (Fig. 3). The method is as follows:
152 a logged section through an architectural element was sub-divided into three sections or ‘windows’
153 of equal thickness (steps 1 and 2, Fig. 3). Where a window boundary fell within a bed, the boundary

154 was moved to the closest base or top of the nearest sandstone bed. The proportion of sandstone
 155 that the thickest and thinnest beds constituted in a window was calculated (step 3, Fig. 3). An
 156 average of the two was taken and converted back to a thickness (step 3 Fig. 3). The bed with a
 157 thickness that most closely corresponded to this calculated thickness was chosen to be sampled as
 158 an 'average bed' for the succession (step 4, Fig. 3). A sample of the selected bed was collected from
 159 the center of the bed, to avoid the coarse-grained base or fine-grained top. Sampling was designed
 160 to assess sedimentary process controls on the depositional reservoir quality of sandstones within
 161 architectural elements. Therefore, the texture of non-reservoir facies (e.g. mudstones) were not
 162 studied. However, the effects of these potential barriers to flow are considered in architectural
 163 element scale analysis.



165 Figure 3: The workflow for a repeatable stratigraphic sampling method. Vertical scale in meters.

166

167 Thin-sections were point-counted using a petrographic microscope at 300 points per section
168 (step 5, Fig. 3). The Gazzi-Dickinson method was used to determine composition (Gazzi, 1966;
169 Dickinson, 1970; Ingersoll et al., 1984). The grain-size was determined by measuring the long axes
170 of optically distinguishable grains. The median and D90 (90th percentile) grain-sizes are used for
171 analysis as mean results were skewed by mudstone chips in some samples. Sorting was determined
172 following Folk and Ward (1957) by measurement of the long and short axis of optically resolvable
173 detrital grains. Detrital and authigenic clays were not distinguishable in thin-section; therefore,
174 there is some uncertainty in inferring initial detrital clay contents. However, it is recognized that
175 proportions of detrital matrix content in modern turbidites is variable between different bed-types
176 (Sumner et al., 2012; Stevenson et al., 2014a; Stevenson et al., 2014b). Thinner-bedded, finer-
177 grained distal deposits have higher detrital matrix contents compared to comparatively thicker-
178 bedded, coarse grained deposits (Stevenson et al., 2014a; Stevenson et al., 2014b). As the clay
179 content and trends are similar to those observed here the total clay proportion is likely to be a
180 good indicator of original detrital clay content.

181 4.1 Facies

182 Lithofacies are summarized in Table 1 and grouped into facies associations in Table 2:

Table 1: Lithofacies observed in the study area

Facies	Lithology	Sedimentology	Thickness (m)	Interpretation	Facies code
Mudstone	Silty claystone and clayey siltstone	Massive- to weakly-laminated.	0.01 – 2.5	Background sedimentation or deposition from a dilute flow.	LF1
Ripple laminated sandstone	Coarse-siltstone to fine-sandstone, rarely medium-sandstone.	Ripple cross-lamination, typically located in the upper parts of the bed. Climbing ripples locally observed. Commonly produces wavy bed tops.	0.02 – 0.1	Traction plus fallout from a turbulent flow (Allen, 1982; Southard, 1991; Mutti, 1992).	LF2
Planar-laminated sandstone	Very fine- to medium-sandstone.	Laminated sandstone with 0.1 m – 1mm scale alternating coarser – finer laminae. Laminae are typically parallel, rarely sub-parallel. Common coarse-tail grading. Infrequent occurrence of plant fragments and mudstone chips aligned with laminae.	0.04 – 0.5	Layer-by-layer deposition from repeated development and collapse of near-bed traction carpets (Sumner et al., 2008) and migration of low-amplitude bed-waves (Best and Bridge, 1992; Sumner et al., 2008).	LF3

Structureless sandstone	Very fine- to medium-sandstone, rare coarse-sandstone.	Typically structureless and commonly normally-graded or coarse-tail graded. Occasional mudstone chips occur, typically in fine- to coarse-sandstone beds. <i>Nummulites</i> are infrequently observed.	0.05 – 0.5	Rapid settling from a high concentration flow under hindered settling conditions (e.g. Sanders, 1965; Lowe, 1982; Mutti, 1992).	LF4
Mm-spaced laminated sandstone	Medium- to coarse-sandstone.	Laminated sandstone, laminae are 5 – 15 mm thick, parallel to sub-parallel and typically coarser-grained than surrounding sandstone. Coarser laminae are typically inversely graded.	0.1 – 0.5	Repeated collapse of traction carpets below a high-density turbidity current (e.g. Mutti, 1992; Cartigny et al., 2013), or kinetic sieving within the traction carpet (e.g. Talling et al., 2012).	LF5
Cross-bedded sandstone	Medium- to very coarse-sandstone	Centimeter- to decimeter-scale cross stratification. Foresets commonly contain clasts of mudstone or detrital material, with maximum grain-sizes of approximately 20 cm. The size of clasts reduces vertically up	0.4 – 0.65	Bed reworking by long-lived flows with relatively low depositional rates and near-bed concentrations which bypassed basin-ward (Allen and Friend, 1976; Mutti, 1992; Baas et al.,	LF6

		foresets. Transition gradually to planar laminated sandstone over 5 – 10 cm at the top.		2004; Baas et al., 2011; Talling et al., 2012).	
Conglomerate	Poorly sorted clasts of pebbles and cobbles, with infrequent boulders (max. 36 cm). Poorly sorted sandstone matrix.	Clast supported structureless deposit. Often subtle grading is present in the upper 30 cm. Clasts are usually sub- to well-rounded and include lithic fragments, quartz, limestone, mudstone and flint.	0.35 – 1.3	Deposition from a highly concentrated flow under hindered settling conditions (e.g. Walker, 1975; Lowe, 1982), or frictional freezing (Mutti, 1992).	LF7
Matrix-supported chaotic deposits	Poorly-sorted, clast-rich matrix consisting of sandstone, siltstone and mudstone.	0.2 – 25	0.2 – 25	Clast-rich, poorly-sorted, matrix supported beds are suggestive of <i>en-masse</i> deposition from laminar (debris) flows with a high yield strength (e.g. Nardin et al., 1979).	LF8

Table 2: Facies associations observed in the study area

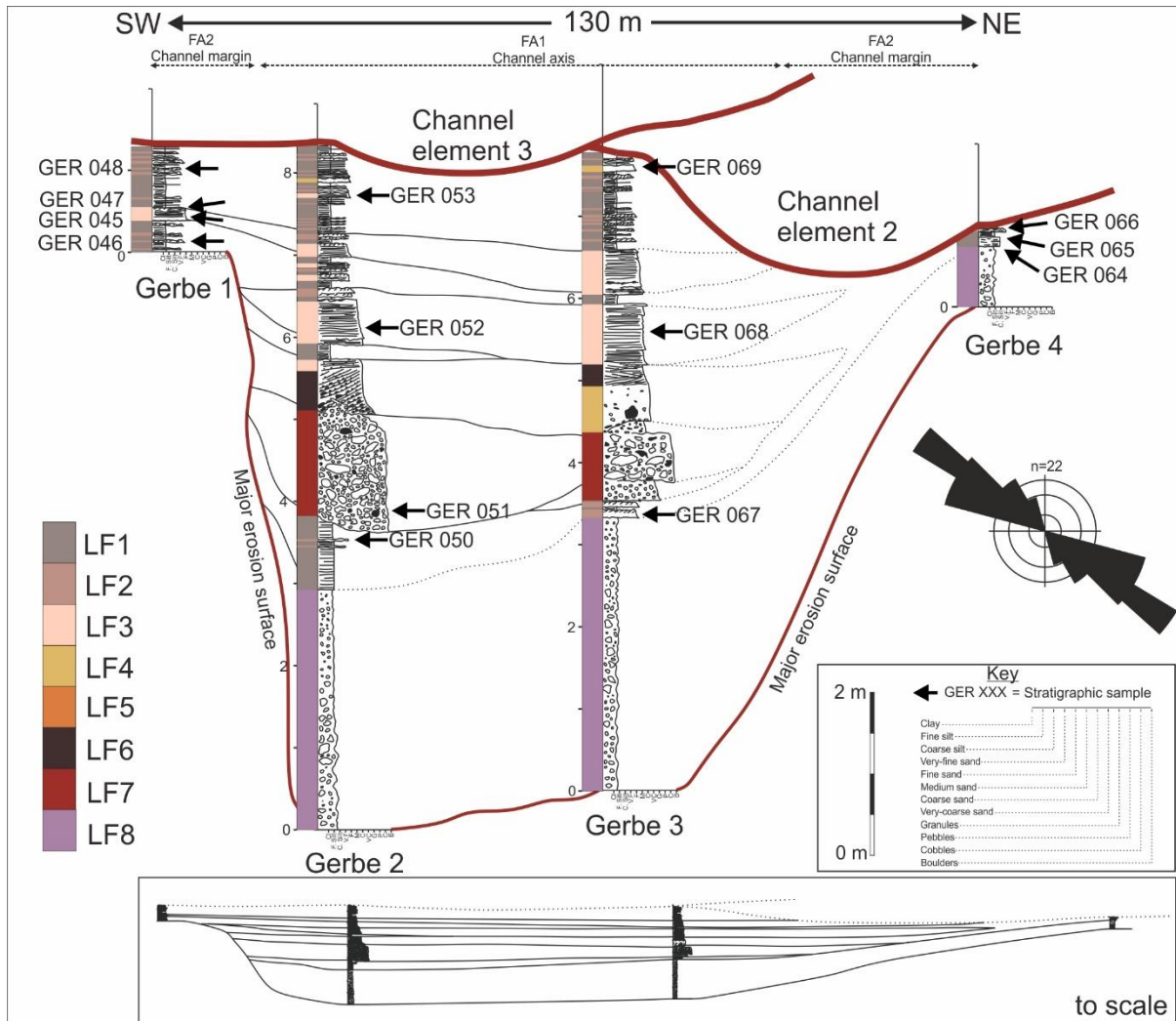
Facies association	Description	Interpretation
FA1	<p>An overall thinning- and fining-upwards succession 7 – 9 m thick which fill a basal incision surface. Characterized by: LF8 at the base overlain by interbedded LF2 and LF1; a sharp erosive contact to amalgamated LF7; a sharp, erosive contact to thick-bedded, amalgamated LF3, LF4 and LF6 containing abundant mudstone chips and lithic-fragments derived from LF7; a thinning- and fining-upward succession of thin-bedded, non-amalgamated LF3 and LF2.</p>	<p>Overall thinning- and fining-upward succession filling an incision is consistent with channel axis deposits (e.g. Mutti, 1977; Clark and Pickering, 1996; Campion et al., 2000; Sullivan et al., 2000; Beaubouef, 2004; McHargue et al., 2011; Hubbard et al., 2014; Li et al., 2016).</p>
FA2	<p>Thin-bedded and non-amalgamated LF3 and LF2 0.3 – 1.5 m thick. LF8 may be locally present at the base of the association. Beds are predominantly tabular and pass laterally into FA1.</p>	<p>Thin-bedded deposits which are adjacent to, and pass into, thicker –bedded deposits of FA1. Consistent with channel margin deposits described elsewhere (Mutti, 1977; Clark and</p>

		Pickering, 1996; Campion et al., 2000; Eschard et al., 2003; Beaubouef, 2004; Hubbard et al., 2014; Li et al., 2016).
FA3	Commonly amalgamated packages of LF4 and LF3, with localized LF5, 4 – 6 m thick. Localized scouring on a centimeter- to meter-scale, however bed geometries are typically tabular over 10's – 100's meters.	Thick-bedded, structureless, laterally extensive beds which transition to thinner-bedded deposits on a 0.1 – 1 km scale and form packages several meters in thickness are consistent with lobe axis deposits (Prélat et al., 2009; Grundvåg et al., 2014; Marini et al., 2015).
FA4	Interbedded, infrequently amalgamated medium- and thin-bedded LF3 and LF2 packages 4 – 6 m thick. LF4 is infrequently observed. Beds typically have a sharp base and sharp top overlain by LF1. Localized, decimeter-scale scouring is observed, however beds are predominantly tabular at outcrop-scale.	Medium- and thin-bedded structured sandstones deposited predominantly from low-density turbidity currents which form meter-scale packages are consistent with lobe off-axis deposits (e.g. Prélat et al., 2009).

FA5	Thin-bedded sandstone and siltstone packages 1 – 2.5 m thick dominated by LF2 and interbedded with LF1. LF3 is infrequently observed. Amalgamation is rare. Beds typically exhibit a sharp base, and sharp top overlain by LF1. Bed geometries are tabular to wavy.	Thin-bedded, rippled, sandstones deposited by dilute low-density turbidity currents are commonly identified in lateral lobe fringe deposits (e.g. Pr�lat et al., 2009; Grundv�g et al., 2014; Marini et al., 2015; Kane et al., 2017; Spsychala et al., 2017b). Similar facies in the Jaca Basin have previously interpreted as lobe-fringe by Mutti (1977).
-----	---	--

189 **5.1 Architectural element interpretations**

190 The geometrical relationships established in the stratigraphic correlations of Figures 4
 191 and 5, and the facies associations described in Table 2, are used to interpret the environment of
 192 deposition of the Gerbe and Broto architectural elements.



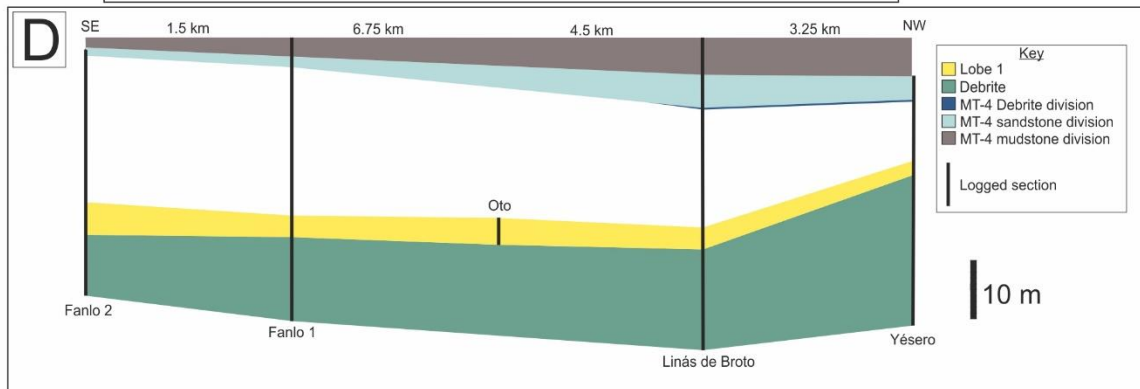
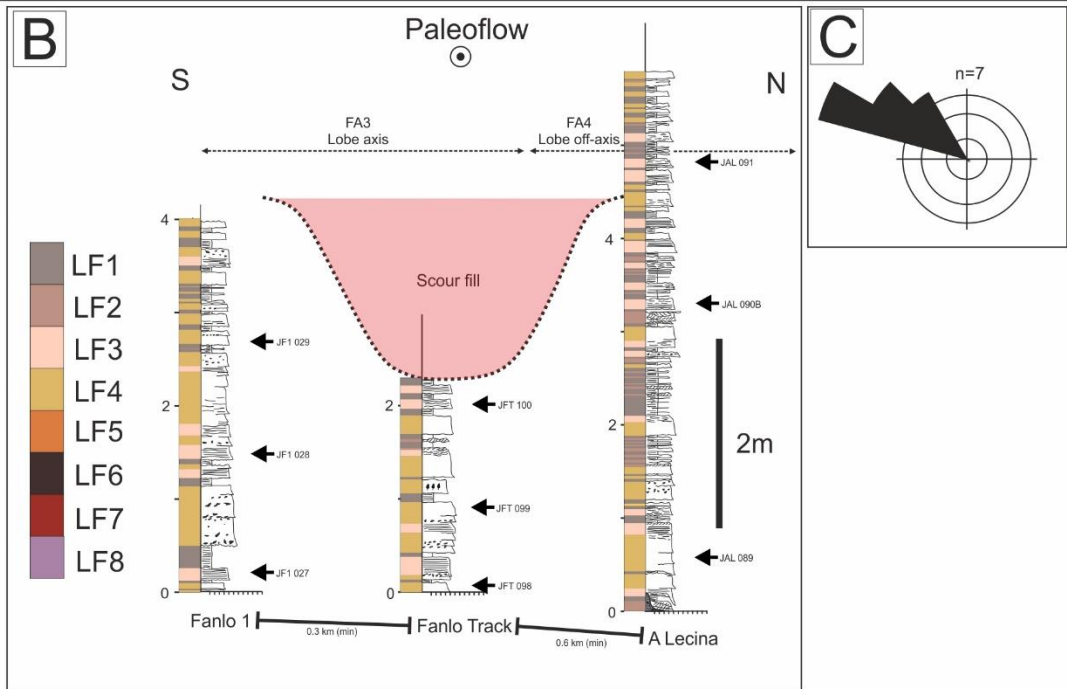
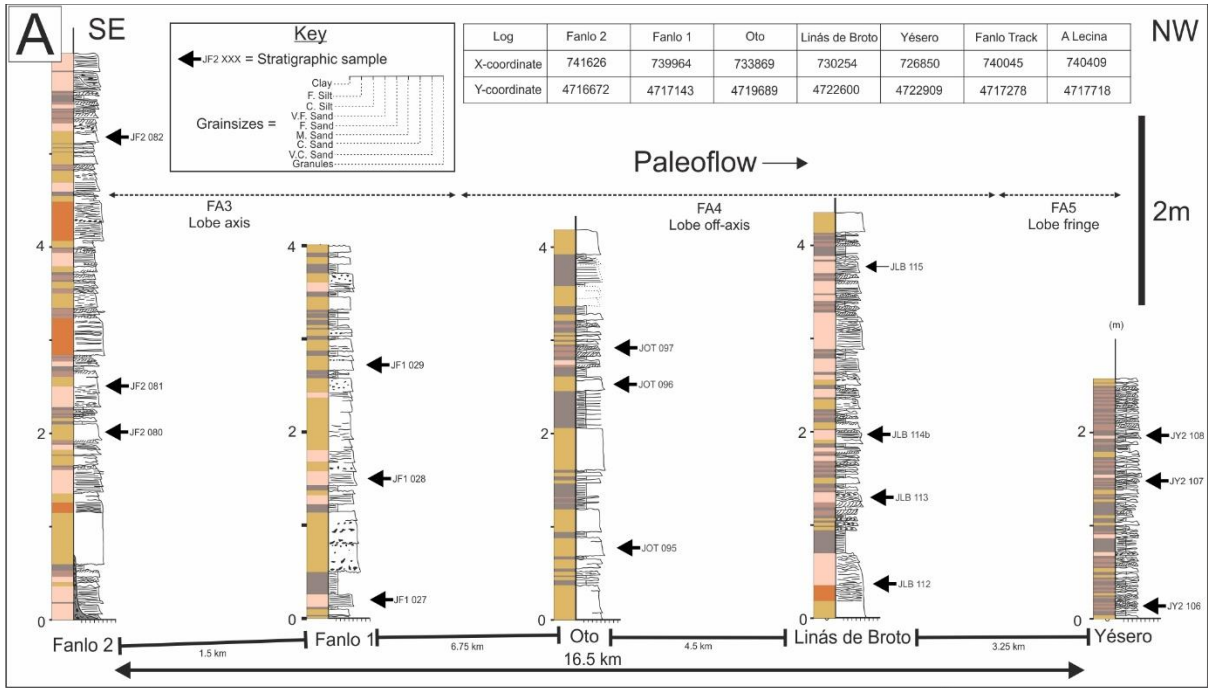
193
 194 Figure 4: Architectural panel of the Gerbe channel-fill element (channel-fill element 1 of this complex). The
 195 orientation is broadly across depositional strike based on geometry and paleocurrent analysis. The channel-
 196 form is defined by a major basal erosion-surface. This is overlain by a debris attributed to channel-
 197 excavation. The channel-fill has two main facies associations, FA1 and 2. The channel axis, FA1, is
 198 characterized by an overall thinning- and fining-upwards succession overlying LF8. The channel margins,
 199 FA2, are characterized by thin-bedded low-density turbidites.

200 5.2 Gerbe architectural element

201 The Gerbe channel-fill element is approximately 150 m wide, representing a near complete
202 across depositional-strike transect as indicated by paleocurrent measurements (Fig. 4), and exhibits
203 marked lateral facies changes between log localities (Fig. 4). The measured sections at localities
204 (localities refer to measured sections herein) Gerbe 2 and Gerbe 3 are 8.5 m and 7.9 m thick
205 respectively and are characterized by FA1 (Figs. 4, 6B and D). The Gerbe 1 and Gerbe 4 localities
206 are 1.4 m and 1.1 m, respectively, and are characterized by FA2 (Figs. 4, 6A).

207 5.3 Broto architectural element

208 The Broto lobe (Lobe 1 of Bell et al., *in press*; Fig. 5), has a comparatively tabular geometry
209 and is approximately 16 km in length and more than 0.9 km wide (Fig. 5A, B). The element exhibits
210 more-gradual lateral facies changes compared to the Gerbe channel-fill element (Fig. 5A, B). The
211 base and top of the architectural element are marked by a debrite (Figs. 5D, 6E) and a laterally
212 persistent thin-bedded package that can be correlated on a kilometer-scale between outcrops (Fig.
213 6G), respectively. The Fanlo 1, Fanlo 2 and Fanlo Track localities predominantly consist of FA3,
214 and are interpreted as lobe axis deposits (Fig. 5, 6E; e.g. Prélat et al., 2009). The A Lecina, Oto and
215 Linás de Broto localities are characterized by FA4 and are interpreted as lobe off-axis (Fig. 6F; e.g.
216 Prélat et al., 2009). The Yésero locality consists of FA5 and is interpreted as the lobe fringe (Fig.
217 6H; e.g. Prélat et al., 2009). The observed facies changes and geometries are consistent with lobes
218 observed elsewhere (e.g. Prélat et al., 2009; Grundvåg et al., 2014; Marini et al., 2015; Kane et al.,
219 2017; Sychala et al., 2017a), and have previously been interpreted as lobes within the Jaca Basin
220 (Mutti, 1977; Mutti, 1992; Bell et al., *in press*).



222 Figure 5: Architectural panels of Lobe 1 of the Upper Broto system: A) Depositional-dip correlation of
223 Lobe 1, from lobe axis at Fanlo 2 to frontal lobe fringe at Yésero; B) Depositional-strike architecture of
224 Lobe 1, from lobe axis at Fanlo 1 and Fanlo Track to lobe off-axis at A Lecina; C) Paleocurrents measured
225 in Lobe 1 suggest flow to the northwest, consistent with other studies within the basin (e.g. Mutti 1977,
226 1984, Remacha et al., 2005, Bell et al., *in press*); D) Stratigraphic context of down depositional-dip correlation
227 panel showing Lobe 1 in relation to key marker beds (modified from Bell et al., *in press*).

228 Gradual facies changes over 100's – 1000's meters in Lobe 1 contrast to distal deposits of
229 the Upper Broto System (i.e. the basin plain, *sensu* Remacha et al., 2005). Northwest of Jaca (Fig.
230 1A) basin-plain deposits exhibit more tabular cross-sectional geometries, with less lateral
231 variability, and do not form lobes (Remacha and Fernández, 2003; Remacha et al., 2005; Bell et al.,
232 *in press*). An idealized basin-plain bed comprizes: a clean basal sandstone, overlain by a clast-rich,
233 poorly-sorted division, followed by a thick mudstone cap with an upper-carbonate-rich division
234 (Remacha and Fernández, 2003; Remacha et al., 2005; Bell et al., *in press*). Bases of basal clean
235 sandstone divisions have flute and tool marks suggesting flow to the west/northwest. Upper
236 surfaces of some sandstone beds have ripple cross laminations suggesting paleoflow to the north,
237 interpreted to form due to flow deflection from the southern, carbonate slope (Remacha and
238 Fernández, 2003; Remacha et al., 2005; Bell et al., *in press*). Poorly sorted divisions are interpreted
239 to form either through: repeated deposition and liquefaction of lamina from bores within deflected
240 turbulent flows (Remacha and Fernndez, 2003, Remacha et al., 2005); or from turbulent flows
241 which collapsed to form predominantly laminar flows during flow deflection (Bell et al., *in press*).

242 **6.1 Results**

243 Architectural and textural data were collected for both the channel-fill element and lobe. Textural
244 properties are split into facies associations for each architectural element to enable comparison of
245 architectural and textural properties, and consequent depositional reservoir quality in different sub-
246 environments within deep-water systems.



249 Figure 6: A) Channel-margin facies: structured sandstones and siltstones deposited from low-density
250 turbidity currents; B) Channel-axis facies, from the base: pebbly mudstone, conglomerate and cross-bedded
251 sandstone. The cross-bedded sandstone has an erosional base and overlies the conglomerate, with evidence
252 for substrate entrainment; C) Channel-margin siltstones overlying pebbly-mudstone; D) Channel-axis
253 pebbly-mudstone erosively overlain by thick-bedded sandstone; E) Amalgamated, thick-bedded lobe axis
254 sandstones. Onlap of beds onto the underlying debrite is observed to the right of the hammer (length 28
255 cm); F) Medium-bedded lobe off-axis; G) Thin-bedded package overlying Lobe 1 at Fanlo 2. Top of Lobe
256 1 is at the base of the hammer; H) Thin-bedded lobe-fringe sandstones and siltstones at Yésero.

257 **6.2 Composition**

258 **6.2.1 Siliciclastic detrital grains**

259 Non-carbonate detrital grains consist of: monocrystalline quartz (6% – 23.7%), polycrystalline
260 quartz (up to 4.3%), plagioclase feldspar (up to 14.3%), K-feldspar (trace), sedimentary rock
261 fragments (up to 3.3%), metamorphic rock fragments (up to 3.7%), igneous rock fragments (up to
262 3.7%), muscovite (up to 1.3%) and trace minerals.

263 **6.2.2 Carbonate detrital grains**

264 Carbonate grains are common and can make up the largest group of detrital grains within a
265 sample (6.3 – 27.3%). Carbonate grains consist of dolostone, sparitic limestone, micritic limestone,
266 peloids, aggregate grains and fossils. Fossils identified in thin section include foraminifera (benthic
267 and planktonic), gastropods, algae and echinoderm fragments.

268 **6.2.3 Authigenic minerals**

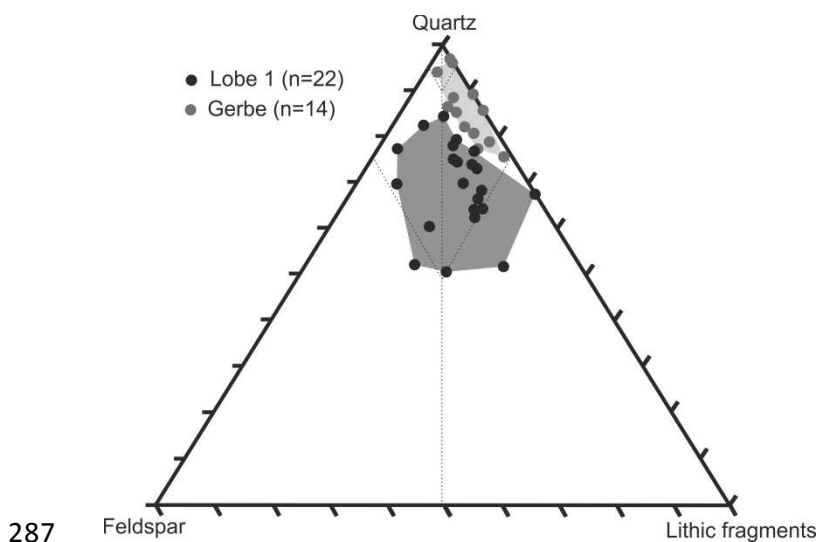
269 Calcite is the dominant authigenic mineral within the samples (19.7% – 38.3% of grains
270 counted), present as both pore-filling cement and replacement of detrital grains. Minor amounts
271 of authigenic quartz (typically <5%, but locally up to 12%) are identified, typically as overgrowths
272 or pore-filling cement. Traces of authigenic plagioclase and oxide minerals are present, typically
273 <1%.

274 **6.2.4 Matrix minerals**

275 Matrix-mineralogy is not optically resolvable. However, where present, matrix is typically
276 identified between or coating larger grains. Pseudomatrix consisting of ductile grains (typically
277 mudstone or micritic limestone) is commonly observed within samples.

278 **6.2.5 Classification**

279 A standard ternary plot of quartz-feldspar-lithic fragments indicates that most samples are
280 categorized as sublitharenites (Fig. 7; see also: Das Gupta and Pickering, 2008; Caja et al., 2010).
281 Linked channel and lobe deposits are shown to exhibit compositional differences (e.g. Stalder et
282 al., 2017). Here, Gerbe samples are more quartz-rich, with some classified as quartz arenites,
283 whereas Broto samples are more feldspar-rich (Fig. 7). This study primarily concerns textural
284 properties and trends, and so composition is not discussed in depth. Compositional evolution,
285 classification and provenance within the Hecho Group are reported in Fontana et al. (1989), Zuffa
286 et al. (1995), Das Gupta and Pickering, (2008), and Caja et al. (2010).



288 Figure 7: QFL (Quartz, Feldspar, Lithic fragments) plots from the 36 point-counted thin-sections, assigned
289 to each study area. Most samples are classified as sub-litharenites. However, the Gerbe samples are typically
290 more quartz-rich and feldspar-poor compared to Lobe 1 samples. Ternary plot after Pettijohn et al. (1972).

291

292 Table 3: Architectural and textural properties at each logged section.

Basin	Locality	Net sandstone thickness (m)	Sandstone %	%Amalgamate d	Median grain-size (mm)	D90 (mm)	Sorting (F&W)	Mean matrix%	Mean authigenic %
Aínsa	Gerbe 1	0.425	31.3	14.286	0.090	0.127	0.225	25.675	31.900
Aínsa	Gerbe 2	3.360	39.3	15.385	0.098	0.161	0.181	19.633	39.467
Aínsa	Gerbe 3	3.680	46.5	39.394	0.109	0.155	0.205	14.433	47.667
Aínsa	Gerbe 4	0.040	3.6	0.000	0.041	0.053	0.245	34.333	36.900
Jaca	Fanlo 2	5.510	90.0	78.378	0.150	0.212	0.204	7.556	36.111
Jaca	Fanlo 1	3.100	77.1	67.742	0.175	0.285	0.134	8.556	31.222
Jaca	Oto	2.895	68.9	38.095	0.096	0.141	0.188	15.778	35.889
Jaca	Linás de Broto	3.220	73.7	34.091	0.166	0.316	0.199	15.833	33.417
Jaca	Yésero 2	1.385	54.1	3.636	0.056	0.079	0.174	29.000	32.444
Jaca	A Lecina	3.945	67.3	28.571	0.169	0.235	0.208	15.444	36.333

Jaca	Fanlo	1.750	76.1	62.500	0.250	0.369	0.173	8.433	37.900
	Track								

293 Table 4: Architectural and textural properties of facies associations

Basin	Sub-environment	Avg. sandstone thickness (m)	Avg. sandstone %	Avg. %amalgamated	Avg. median grain-size (mm)	Avg. D90 (mm)	Avg. sorting (F&W)	Avg. matrix%	Avg. mean authigenic %
Aínsa	Channel-axis	3.520	42.9	27.389	0.103	0.158	0.193	17.033	43.567
Aínsa	Channel-margin	0.233	17.4	7.143	0.065	0.090	0.235	30.004	34.400
Jaca	Lobe axis	3.453	81.1	69.540	0.192	0.289	0.170	8.181	35.078
Jaca	Lobe off-axis	3.353	70.0	33.586	0.143	0.230	0.198	15.685	35.213
Jaca	Lobe fringe	1.385	54.1	3.636	0.056	0.079	0.174	29.000	32.444

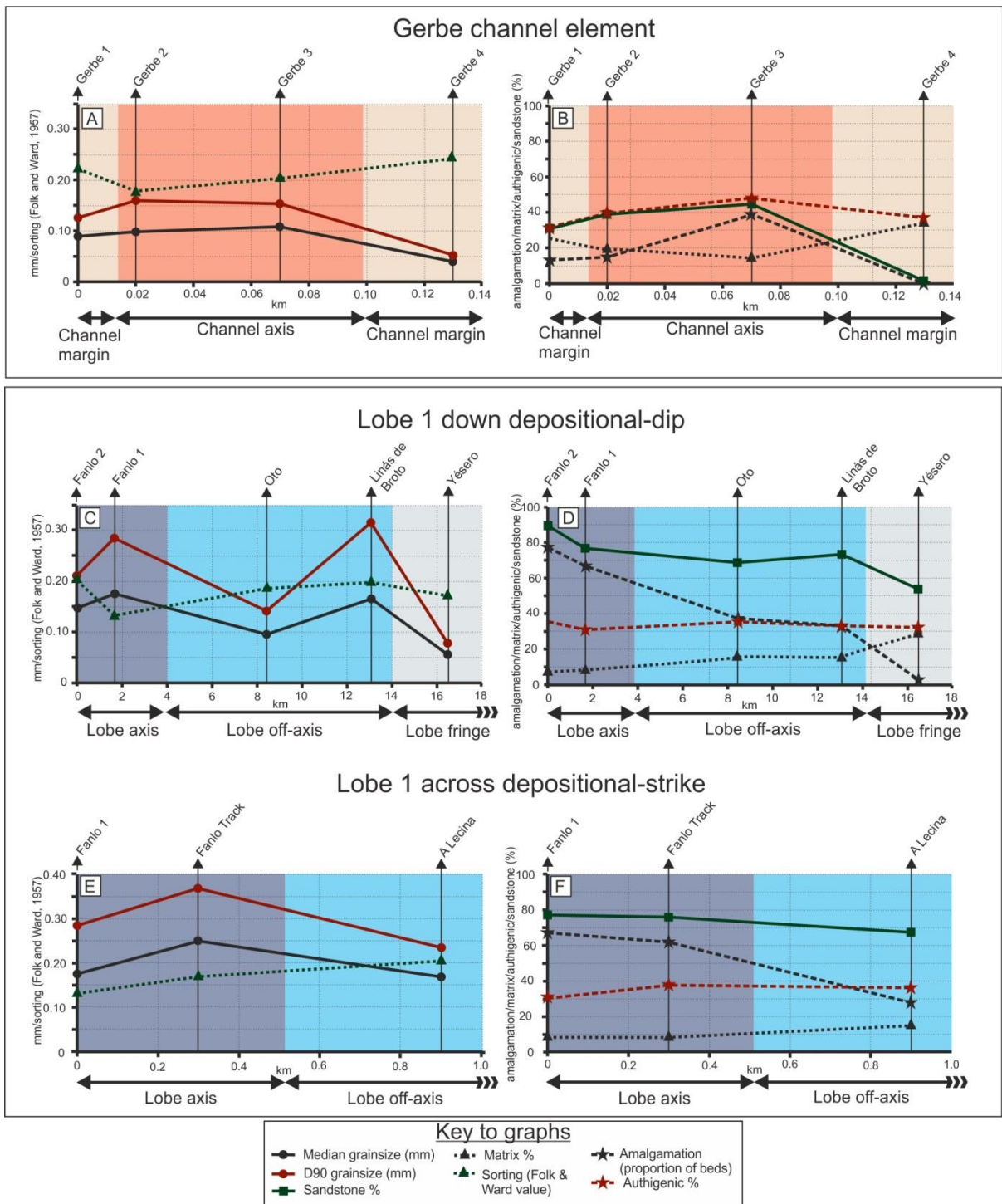
295 6.3 Gerbe Channel-fill element

296 6.3.1 Architectural- and bed-scale data

297 The thickness of the Gerbe channel-fill element increases from Gerbe 1 and 4 to Gerbe 2
298 and 3 respectively (Fig. 4). The proportion of amalgamated sandstone beds is similar between the
299 channel-margin at Gerbe 1 and channel-axis at Gerbe 2; however, the amalgamation ratio is higher
300 at Gerbe 3, and lower at Gerbe 4 (Figs. 8B; Tables 3, 4). Sandstone-percentage is similar in the
301 channel-axis and channel-margins due to the debrite located in the channel-axis, however the total
302 thickness of sandstone is greater in the channel-axis (Fig. 8B; Table 4).

303 6.3.2 Lateral variation in texture

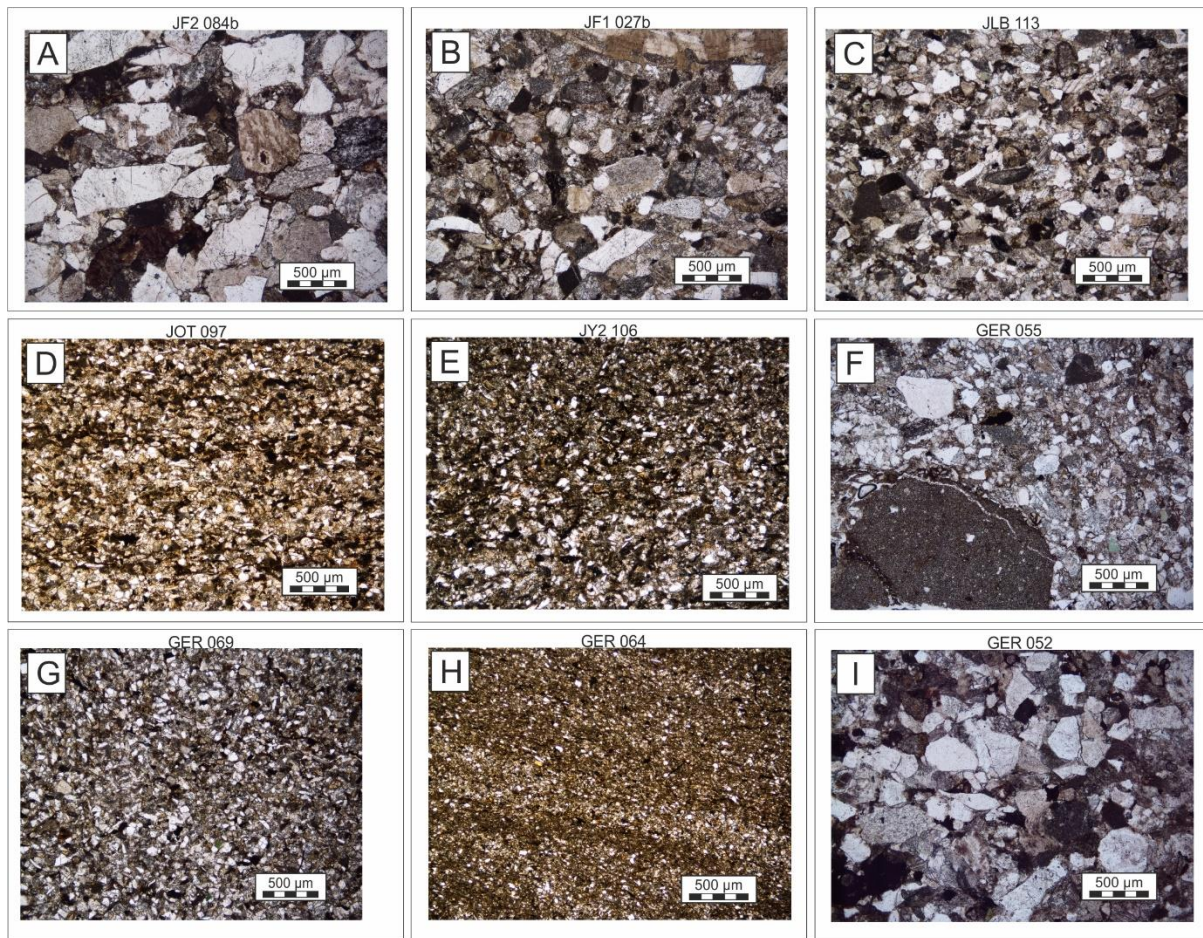
304 Grain-size varies within the channel-fill sandstones (Figs. 8A, 9; Table 3). The median
305 grain-size slightly increases from the western channel-margin Gerbe 1, into the channel-axis
306 deposits of Gerbe 2 and 3 (440 $\mu\text{m}/\text{km}$; Figs. 8A, 10; Table 3). Median grain-size then decreases
307 to the eastern channel-margin at Gerbe 4 (1130 $\mu\text{m}/\text{km}$; Fig. 8A; Table 3). The D90 (90th percentile
308 of grain-size) shows a similar trend, increasing from Gerbe 1 to Gerbe 2 and 3 (1700 $\mu\text{m}/\text{km}$; Figs.
309 8A, 10; Table 3). The D90 at Gerbe 4 is finer than in other positions (Fig. 8A; Table 3). The
310 optically-resolvable detrital grains of the channel-margin deposits are better sorted compared to
311 the channel-axis deposits (Fig. 8A Table 3). The authigenic mineral content increases from the
312 channel-margins into the channel-axis positions (Fig. 8B; Table 4). Channel-margin deposits at
313 Gerbe 1 and 4 have higher matrix content compared to channel-axis deposits at Gerbe 2 and 3
314 (Fig. 8B; Tables 3, 4). Matrix content increases from Gerbe 2 to 1, and Gerbe 3 to 4 at a rate of
315 310 %/km and 340 %/km respectively (Fig. 10).



316

317 Figure 8: Spatial variation in textural and architectural properties within Lobe 1 and the Gerbe channel-fill

318 element.



320

321 Figure 9: Example grain-scale textures of lithofacies: A) High-density turbidite from lobe axis setting; B)
 322 High-density turbidite from lobe axis setting. A foram test is present at the top of the sample; C) Low-
 323 density turbidite from lobe off-axis setting; D) Low-density turbidite from lobe off-axis setting; E) Low-
 324 density turbidite from lobe fringe setting; F) Channel-axis conglomerate, with large fine-grained dolostone
 325 clast; G) Low-density turbidite from channel-axis setting; H) Ripple cross-laminated low-density turbidite
 326 from channel-margin setting; I) High-density turbidite from channel-axis setting.

327

328

329 6.3.3 Vertical textural variation

330 Textural properties also vary vertically within the Gerbe channel-fill element (Figs. 9, 11).

331 Overlying the basal debrite, channel-axis deposits show an increase in grain-size (both median and

332 D90) from thin-beds (>4 m on Figs. 11A, B) into the thicker-bedded, amalgamated conglomerate
333 and sandstone (2 – 4 m on Figs. 11A, B). There is a fining upward profile into the thinner-bedded
334 deposits in the upper 2 m (Figs. 11A, B). Channel-margin positions show a general fining upward
335 trend in both median and D90 grain-sizes (Figs. 11A, B). Sorting improves upwards in both
336 channel-axis and channel-margin deposits (Fig. 11B), a decrease in sorting at 5.2 m at Gerbe 2 is
337 observed within the conglomerate sample. There is no clear trend to vertical variation in authigenic
338 mineral content, however an upward decrease is observed at Gerbe 1 (Fig. 11D). There is a general
339 upward increase in matrix content at all positions (Fig. 11E). At channel-axis positions matrix
340 content decreases from the lower thin-bedded deposits into the thick-bedded amalgamated
341 sandstones located between 2 and 4 m (Fig. 11E). Matrix content then shows a general increase
342 upwards into the overlying thinner-bedded deposits (Fig. 11E).

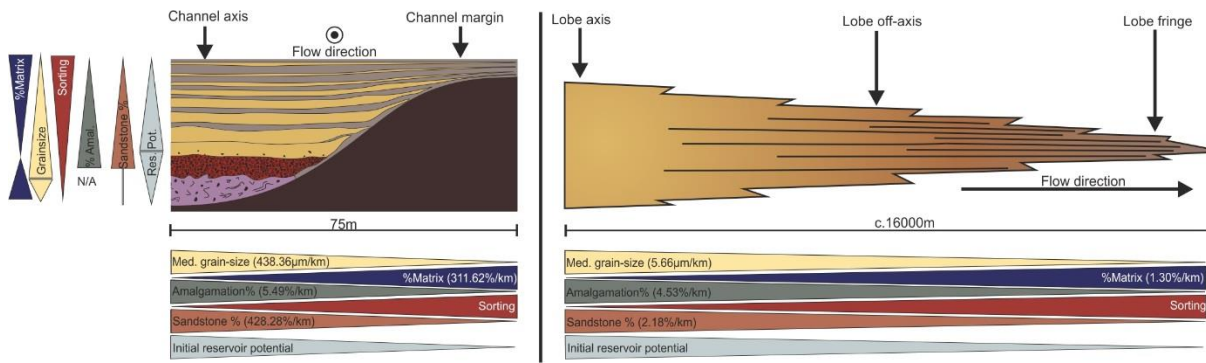
343 6.4 Lobe 1

344 6.4.1 Architectural data

345 The thickness of Lobe 1 decreases from 6.1 m in the most proximal position (Fanlo 2) to
346 2.6 m in the most distal position (Yésero; Fig. 5A). Thickness increases across depositional strike
347 from Fanlo 1 to the lobe off-axis position of A Lecina (Fig. 5B). The proportion of amalgamated
348 beds decreases down-dip from Fanlo 2 to Yésero (4.5%/km; Figs. 8D, 10; Table 3), and across
349 strike from Fanlo 1 to A Lecina (Fig. 8F; Table 3). The degree of amalgamation higher in lobe axis
350 deposits compared to lobe off-axis and lobe fringe deposits (Fig. 8D; Table 4). Sandstone-
351 percentage decreases from Fanlo 2 to Yésero (2.8%/km; Figs. 8D, 10; Table 3). Across-strike, the
352 sandstone-percentage decrease from Fanlo 1 to A Lecina is 1

353 ess pronounced (Fig. 8F; Table 3). Lobe axis deposits exhibit a higher sandstone
354 proportion than lobe off-axis and lobe fringe deposits (Table 4).

355



356

357 Figure 10: Schematic illustration of the spatial variation in architectural and textural properties within deep-
 358 water channel-fill elements and lobes. Within the lobe, textural and architectural properties vary most-
 359 strongly laterally. The channel-fill element shows strong trends in textural and architectural properties both
 360 laterally and vertically. The inferred reservoir quality decreases from lobe axis to lobe fringe, and from
 361 channel-axis to channel-margin. Reservoir quality also decreases vertically within the Gerbe channel-fill
 362 element, if the basal non-reservoir debrite is not included. The lateral gradient of change in properties is
 363 typically around two orders of magnitude greater within the channel-fill element compared to the lobe.

364

365 6.4.2 Textural data

366 Textural properties vary spatially within Lobe 1 (Figs. 8C and E, 9; Table 3). Overall,
 367 median grain-sizes decrease down-dip from Fanlo 2 to Yésero (6 µm/km; Figs. 8C, 10; Table 3).
 368 Across strike, median grain-size decreases from Fanlo 1 and Fanlo Track, to A Lecina (Fig. 8E;
 369 Table 3). The D90 decreases down-dip from Fanlo 2 to Yesero (5 µm/km; Figs. 8A, 10; Table 3).
 370 D90 increases northwards, across strike from Fanlo 1 to Fanlo Track, but is lower at A Lecina
 371 (Fig. 8E; Table 3). In both measurements of grain-size, there is a down-dip increase from Oto to
 372 Linás de Broto (Fig. 8C; Table 3). Sorting is relatively consistent throughout Lobe 1, with most
 373 samples categorized as moderately or moderately-well sorted (Figs. 8C, E; Table 3; *sensu* Folk and
 374 Ward, 1957).

375 The proportion of authigenic minerals shows little variation across Lobe 1 (Fig 8D, F;
 376 Table 3). Positions with the highest authigenic mineral contents are in proximal areas (Fanlo 2,

377 Fanlo Track, A Lecina, and Oto; Figs. 8D, F; Table 3); however, Fanlo 1 has the lowest authigenic
378 mineral content (Figs. 8D, F; Table 3). The proportion of matrix increases down-dip from Fanlo
379 2 to Yésero (Fig. 8D; Table 3). Matrix content also increases across-strike from Fanlo 1 to A Lecina
380 (Fig. 8F; Table 3).

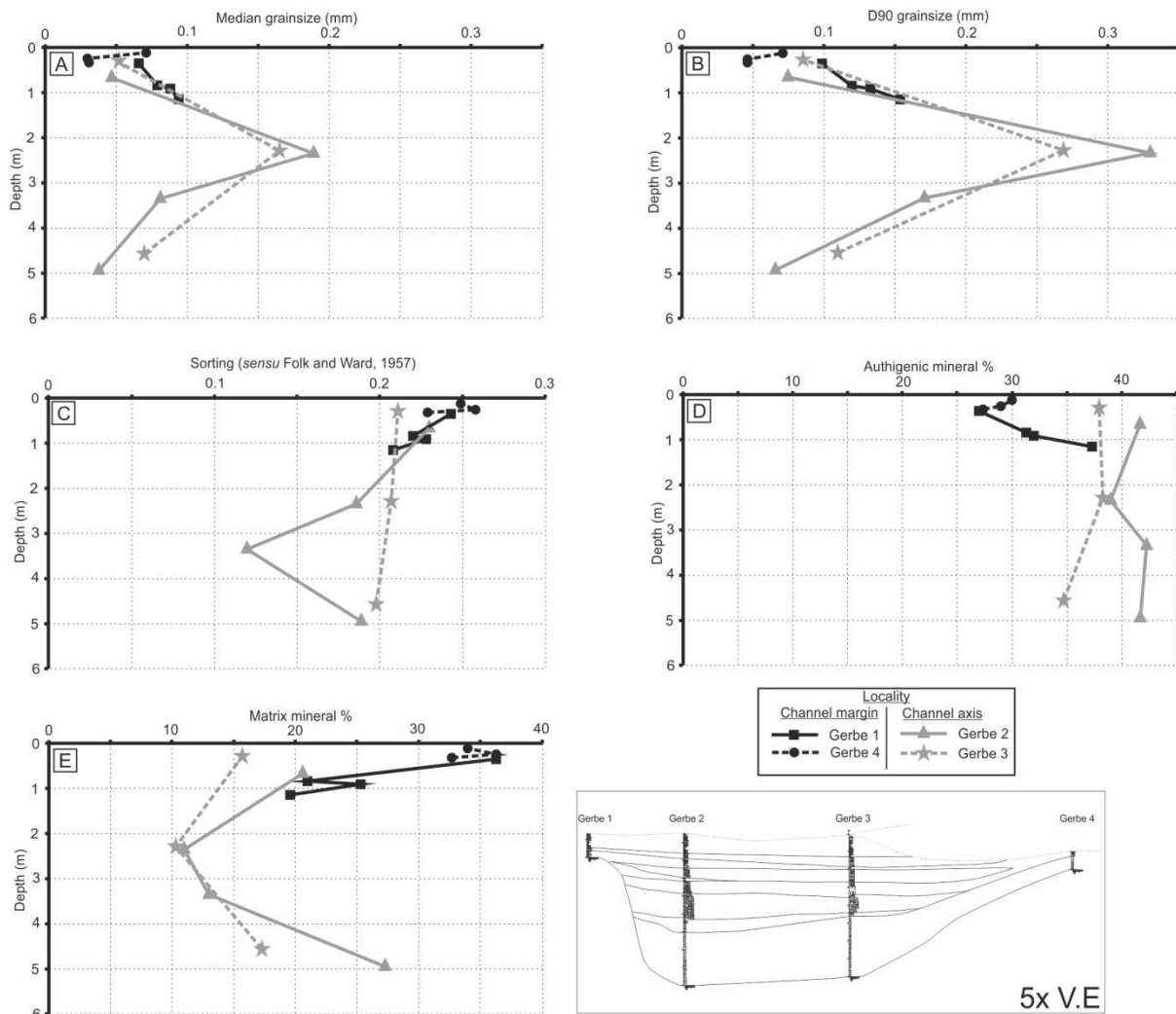
381 Lobe axis deposits exhibit the coarsest median grain-sizes compared to lobe off-axis and
382 lobe fringe deposits (Figs. 8C and E, 9; Table 3); and coarser D90 grain-sizes compared to lobe
383 off-axis deposits (Figs. 8C and E, 12B and C; Table 3). The lobe fringe has a much lower D90
384 (Figs. 8C, 12B and C; Table 3). Sorting increases from lobe axis deposits into lobe off-axis deposits,
385 and decreases from lobe off-axis deposits into the lobe fringe deposits (Figs. 8C and E, and 12C
386 and D; Table 4).

387 Lobe axis and lobe off-axis deposits exhibit marginally higher contents of authigenic
388 minerals than the lobe fringe deposits (Fig. 12A; Table 4). Lobe axis deposits exhibit the lowest
389 matrix contents, lobe off-axis deposits have medial matrix contents, and the lobe fringe deposits
390 have the highest matrix content (Figs. 8D and F, 12A, B and D; Table 4). The rate of change is
391 different between the lobe axis and lobe off-axis, and lobe off-axis and lobe fringe. Matrix content
392 increases at 0.6 %/km between Fanlo 2 and Linás de Broto, compared to 3.8 %/km between Linás
393 de Broto and Yesero (Lobe overall increase is 1.3 %/km; Figs. 8D, 10).

394 **6.5 Comparison of textural properties**

395 Scatter plots of textural properties suggest channel-margin and channel-axis deposits have
396 different textural characteristics (Fig. 12). Higher proportions of matrix correspond to lower
397 proportions of authigenic minerals in the Gerbe samples (Fig. 12A). Increased matrix content also
398 corresponds to finer grain-sizes and better sorting of detrital grains in the samples (Fig. 12B, C).
399 Decreases in grain-size are associated with improved sorting of detrital grains, and increased matrix
400 content (Fig. 12B, D). Channel-margin deposits (Gerbe 1 and 4) have fine grain-sizes, high
401 proportions of matrix, low proportions of authigenic minerals and better sorting (Figs. 8A and B,

402 12; Table 4). Comparatively, channel-axis deposits exhibit coarser grain-sizes, lower proportions
 403 of matrix, higher proportions of authigenic minerals, and are more poorly sorted (Figs. 8A and B,
 404 12; Table 4).



405
 406 Figure 11: Vertical variation in textural properties at each Gerbe logged section. The top of each section is
 407 used as a datum. Grain-size typically decreases upwards within the channel fill (A and B). Within the
 408 channel-axis there is an apparent initial increase in grain-size. This is attributed to the upward transition
 409 from a package of thin-beds, interpreted as the deposits of the dilute tails of larger flows which bypassed
 410 the locality, to the main aggradational-fill of the channel. Sorting increases upwards within the channel-fill
 411 (C). The most poorly-sorted sample (~3.2 m Gerbe 2) is a conglomerate (LF6). Vertical changes in
 412 authigenic content are not strongly developed (D). The proportion of matrix increases upwards within the

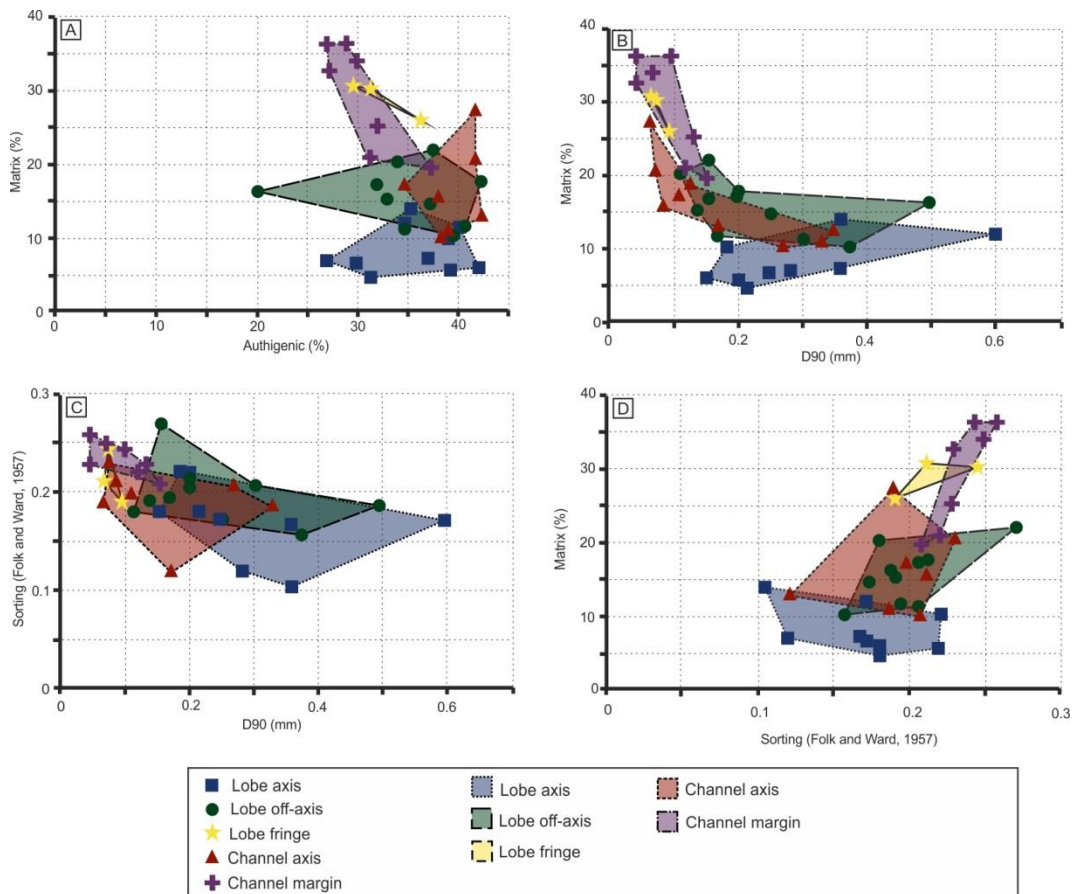
413 channel-fill (E). The initial decrease in the channel-axis represents the transition from the initial bypass-
414 phase to the main aggradational-phase of sand deposition.

415 Lobe 1 exhibits a similar separation of textural properties. Increasing matrix content
416 correlates with decreasing grain-size and better sorting (Fig. 12A, B, D). Matrix and authigenic
417 mineral contents do not exhibit a strong relationship (Fig. 12A). Samples with coarser grain-sizes
418 also exhibit poorer sorting compared to samples with finer grain-sizes (Fig. 12C). Separate
419 groupings of lobe axis, lobe off-axis and lobe fringe samples suggests the sub-environments have
420 distinct textural properties (Fig. 12) although this is likely to form part of a continuum.

421 Comparison of channel-fill element and lobe sub-environment deposits shows similarities
422 between the different architectural elements (Fig. 12). Positions dominated by thinner-bedded
423 deposits (channel-margin and lobe fringe) have finer grain-sizes, higher matrix content, are better
424 sorted and have marginally lower authigenic mineral content compared to positions with thicker-
425 bedded channel-axis and lobe axis deposits (Fig. 12; Table 4). Channel-axis and lobe off-axis
426 deposits show the greatest range in textural properties (Fig. 12; Table 4), especially in grain-size
427 and matrix content (Fig. 12; Table 4).

428 The rate of change of textural properties is typically around two orders of magnitude more
429 abrupt in the channel-fill element (channel axis to channel margin) in comparison to the lobe (Fig.
430 10).

431



432

433 Figure 12: Variation of textural properties within channel and lobe sub-environments. Samples are grouped
 434 by sub-environment interpretations. Channel margin and lobe fringe samples show overlap and consistently
 435 have comparatively finer grain-sizes and higher matrix contents. Channel axis and lobe off-axis samples
 436 overlap and exhibit a mix of grain-sizes and matrix contents. The lobe axis samples typically plot in a discrete
 437 area due to coarser grain-sizes and lower matrix contents.

438 **7.1 Discussion**

439 **7.2 Spatial variation in depositional reservoir quality**

440 The distribution of textural properties (grain-size, sorting and matrix content) within architectural
 441 elements is a first-order control on the initial depositional porosity and permeability of sandstones
 442 (e.g. Fraser, 1935; Beard and Weyl, 1973; Hirst et al., 2002; Lien et al., 2006; Njoku and Pirmez,
 443 2011; Kilhams et al., 2012; Marchand et al., 2015; Porten et al., 2016; Southern et al., 2017) and

444 provides insight into the depositional reservoir quality within the study area. The effects of post-
445 depositional modification are not discussed unless explicitly stated.

446 7.2.1 Gerbe channel-fill element

447 Textural properties vary both laterally and vertically within the Gerbe channel-fill element
448 (Figs. 8, 9, 10, 11, 12). Grain-size increases and matrix content decreases from channel-margins to
449 channel-axis (Figs. 8, 10, 11, 12). In unconsolidated sand, as grain-size increases pore throats
450 become larger and permeability increases (e.g. Beard and Weyl, 1973). However, changes in grain-
451 size do not affect porosity within deposits with the same degree of sorting (Beard and Weyl, 1973).
452 This suggests that initial permeability would have been higher in channel-axis deposits. Grain-size
453 also decreases stratigraphically within the Gerbe channel-fill element (Fig. 11A, B), suggesting
454 initial permeability decreased upwards. Sorting is better in the channel-margins, and also increases
455 vertically within the channel-fill (Figs. 8, 11, 12). Well-sorted deposits exhibit higher porosity and
456 permeability in unconsolidated sand as smaller grains fill intergranular space and block pore throats
457 in poorly-sorted deposits (Beard and Weyl, 1973). However, the overall effect of sorting on
458 reservoir quality is currently inconclusive, as grain-size and clay content often mask its effect (Lien
459 et al., 2006; Porten et al., 2016; *cf.* Njoku and Pirmez, 2011). This is likely an artefact of traditional
460 point counting methods, which calculate sorting data from optically resolvable grains (i.e. not
461 clays). Therefore, channel margin and lobe fringe deposits in which hydraulic fractionation resulted
462 in well-sorted detrital grains, but with a high-matrix content, appear well-sorted. In contrast, the
463 deposits of relatively poorly-stratified, high-density flows are likely to have poorer-sorting of
464 detrital grains, but low-matrix contents. High matrix content in channel margin positions (Figs. 8,
465 10, 11, 12) likely reduced both initial porosity and permeability as detrital clay can impact reservoir
466 quality by blocking pore throats and reducing permeability (Fraser, 1935; Hirst et al., 2002; Lien et
467 al., 2006; Porten et al., 2016). Authigenic mineral content is highest in the channel axis (Fig. 8B),

468 suggesting a higher initial porosity, and that fluid flow was greater in these deposits prior to
469 mesodiagenesis, suggesting higher initial permeabilities.

470 Both sandstone-percentage and the proportion of amalgamated beds decrease from
471 channel-margin to channel-axis (Fig. 8B, 10). Therefore, channel-axis deposits exhibit better
472 depositional reservoir quality at both grain-scale (porosity and permeability) and architectural
473 element scale (sandstone-percentage and amalgamation) compared to channel-margin deposits
474 (Fig. 10).

475 Whilst the depositional reservoir quality of channel-axis sandstones is better compared to
476 the channel margin, the channel-axis in this case contains a thick mudstone-rich debrite. This
477 debrite would have poor reservoir properties (e.g. Hirst et al., 2002), and reduce the overall vertical
478 permeability and depositional reservoir quality of the channel axis. However, incision of channel-
479 fill element one by channel-fill elements two and three improves vertical connectivity of channel-
480 axis sandstones in the channel-complex axis (Fig. 4).

481

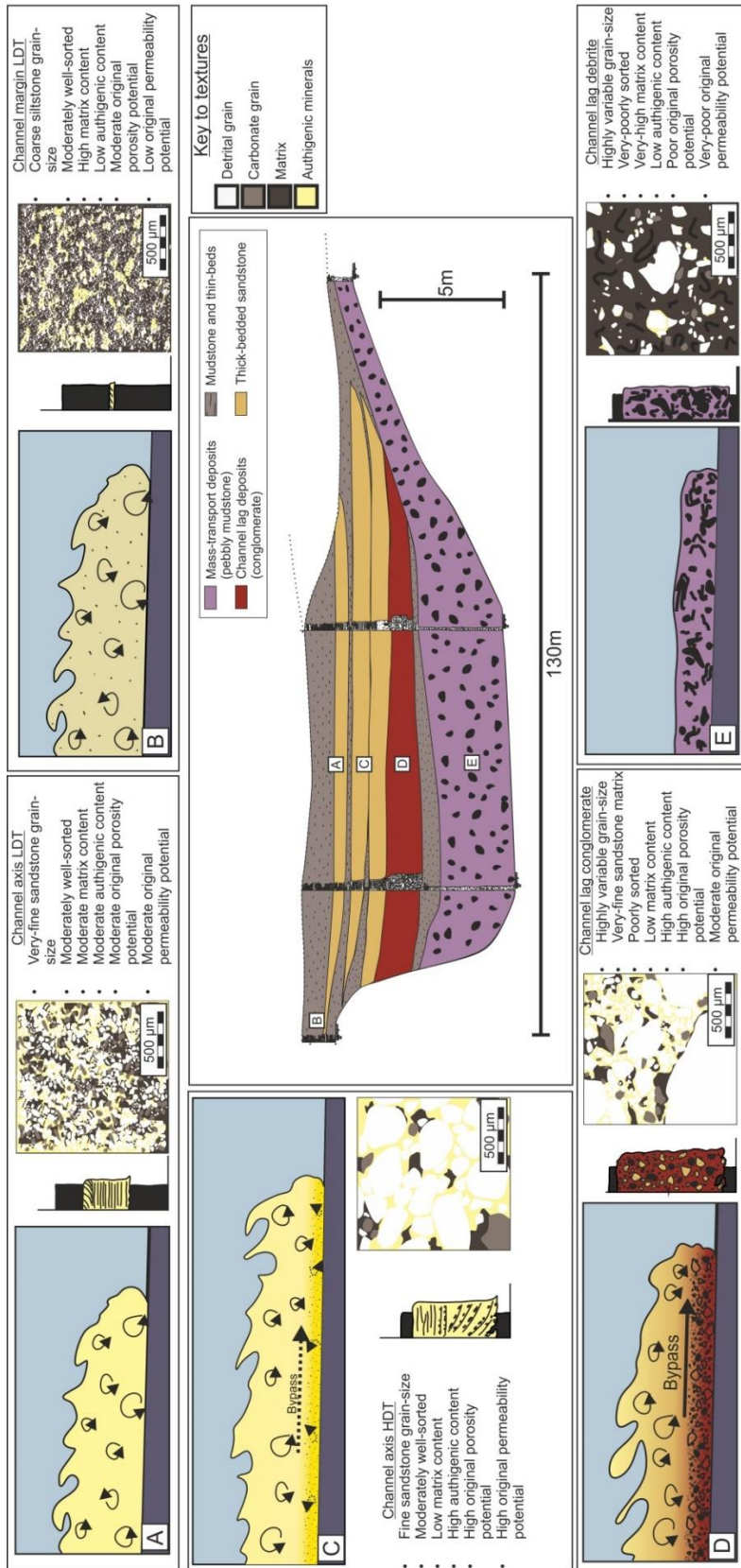
482 *7.2.2 Process controls on depositional reservoir quality distribution*

483 Cycles of channel initiation, incision, and filling record a complicated waxing-waning
484 history of flow energy, and associated sediment bypass and aggradation (e.g. Mutti and Normark,
485 1987; Mutti, 1992; Clark and Pickering, 1996; McHargue et al., 2011; Hubbard et al., 2014;
486 Stevenson et al., 2015). The basal channel surface is interpreted to be excavated by a debris flow,
487 or flows (e.g. Dakin et al., 2013), which deposited the debrite. The debrite is erosively overlain by
488 siltstone and discontinuous thin sandstone beds, interpreted to represent a bypass-dominated
489 channel-base-drape (e.g. Hubbard et al., 2014; Stevenson et al., 2015). Silt-prone drapes act as
490 barriers to flow, but notable detrimental effects are only observed with cross-sectional drape
491 coverages in excess of 60% (e.g. Barton et al., 2010). Subsequent channel-axis aggradation is

492 dominated by amalgamated high-density turbidites (Figs. 4, 13), resulting in high sandstone-
493 percentage and connectivity. The fill progressively thins and fines upward into thin-bedded low-
494 density turbidites (Figs. 4, 13). Channel-margin deposits are characterized almost exclusively by
495 low-density turbidites (Figs. 4, 13). Topography steers high-density turbidity currents more-
496 strongly than low-density turbidity currents (e.g. Al Ja'aidi et al., 2004), and so focussing of high-
497 density turbidity currents within the thalweg concentrates the best reservoir properties in the
498 channel-axis (Figs. 10, 13). Low-density flows, or low-density parts of stratified flows, are able to
499 surmount topography, depositing low-density turbidites contemporaneously on the channel-
500 margin (Fig. 13A, B; e.g. Hiscott et al., 1997). In later stages of channel aggradation, the channel-
501 cut is partly-to-fully filled due to system back-stepping through relative sea-level rise, or other
502 mechanisms, reducing flow-volume and sediment supply to the channel-fill (e.g. Mutti and
503 Normark, 1987; Clark and Pickering, 1996; Campion et al., 2000; Gardner and Borer, 2000;
504 McHargue et al., 2011; Di Celma et al., 2014; Hubbard et al., 2014; Hodgson et al., 2016).
505 Reduction of sediment supply and smaller flow-volume means later flows reaching a given location
506 are finer-grained, more-dilute and have poorer reservoir potential compared to earlier
507 aggradational deposits.

508

509



510

Figure 13: Flow process controls on channel-fill reservoir potential. The lower channel-axis is filled

511

by debris (E), which are poorly-sorted, mudstone-rich and low reservoir potential. Conglomerate (D),

512 representative of a high-concentration, strongly bypassing flow. Reservoir potential in initial channel-axis
513 deposits is high due to amalgamation of high-density turbidites (C and D). Decreases in amalgamation and
514 grain-size, and increases in matrix content vertically and laterally reduce depositional reservoir quality. The
515 upper channel-fill element fill axis (A) and channel-margins (B) are dominated by non-amalgamated low-
516 density turbidites and have poorer grain-scale reservoir potential.

517 7.2.3 Lobe 1

518 Within Lobe 1, the decrease in grain-size from lobe axis to lobe fringe positions (Figs. 8C, 9, 10
519 12) suggests that initial permeability decreased away from the lobe axis. The proportion of matrix
520 increases from lobe axis to lobe fringe (Figs. 8C, 12; see also: Hirst et al., 2002; Marchand et al.,
521 2015; Kane et al., 2017; Fildani et al., 2018), which suggests the lobe-axis exhibited the highest
522 initial porosity and permeability. Trends in sorting are weak in Lobe 1. Lobe off-axis deposits are
523 generally better sorted than both lobe axis and lobe fringes, and therefore the original porosity
524 may have been higher (Fig. 12C, D). However, as grain-size and matrix content are considered
525 stronger controls on reservoir quality (Hirst et al., 2002; Lien et al., 2006; Porten et al., 2016), they
526 are likely to overprint this parameter. At architectural-element scale, the sandstone-percentage and
527 degree of amalgamation decrease away the from lobe axis to the lobe fringe (90 to 54% and 78.38
528 to 3.64% respectively; Figures 8D and F). This suggests lobe-axes had higher reservoir volume and
529 connectivity. Authigenic mineral content is less variable than in the channel-fill element, but is
530 slightly higher in lobe off-axis and lobe axis (Fig. 8D, F), suggesting increased fluid flow during
531 diagenesis. Lobe axis deposits exhibit the best depositional reservoir quality at both grain- and
532 architectural-scales (Fig. 10). Reservoir potential decreases slightly from lobe axis to lobe off-axis,
533 at grain- and architectural-scale (Fig. 10). The relatively abrupt increase in matrix content, decrease
534 in grain-size, decrease in sandstone-percentage and decrease in amalgamation from lobe off-axis
535 to lobe fringe (over a scale of 3.25 km) suggests that depositional reservoir quality and vertical
536 connectivity within lobes decreases considerably from the lobe off-axis to the lobe fringe (Fig. 10).
537 Where lobe fringe successions are reservoir prospects, they are likely to be challenging due to their

538 (relatively) finer grain-size, increased matrix content, reduced thickness and poorer connectivity
539 compared to more proximal positions (Kane and Pontén, 2012; Marchand et al., 2015; Southern
540 et al., 2017; Fildani et al., 2018).

541 *7.2.4 Process controls on depositional reservoir quality distribution*

542 Lobes exhibit lateral facies changes that reflect different sub-environments. Lobe axis
543 deposits are dominated by high-density turbidites, lobe off-axis deposits contain a mixture of high-
544 and low-density turbidites and lobe fringe deposits are dominated by low-density turbidites (Figs.
545 5, 14; e.g. Prélat et al., 2009). Lateral variation of textural properties and composition has been
546 observed in experimental studies (e.g. Middleton, 1967; Garcia, 1994; Gladstone et al., 1998;
547 Hodson and Alexander, 2010; Pyles et al., 2013) and in ancient deposits (Fig. 14; e.g. Hirst et al.,
548 2002; Kane et al., 2017; Lien et al., 2006; Marchand et al., 2015; Porten et al., 2016; Southern et al.,
549 2017; Fildani et al., 2018). Coarse grains are deposited by high-density turbidity currents in
550 proximal positions whereas fines that reach the basin-floor are transported to distal positions in
551 low-density turbidity currents (Fig. 14; e.g. Middleton, 1967). Enrichment of fine-grained material
552 in the lobe fringes may be due to entrainment of substrate in the channel-lobe transition zone, and
553 proximal lobe positions (Kane and Pontén, 2012; Fildani et al., 2018). As grain-size and matrix are
554 strong controls on depositional reservoir quality, their segregation within flow deposits influences
555 reservoir potential distribution within lobes (Figs. 10, 14).

563 turbidites. Lobe-fringe low-density turbidites have fine grain-sizes and higher matrix content, reducing
564 reservoir potential compared to lobe axis and lobe off-axis deposits.

565 **7.3 Implications of detrital matrix distribution**

566 Detrital matrix and ductile grains have a negative effect on the depositional reservoir
567 quality by blocking pore throats (e.g. Fraser, 1935), and during compaction by forming a
568 pseudomatrix (e.g. Marchand et al., 2015). However, clay coatings (predominantly chlorite) on
569 grains can also act to preserve porosity and permeability by inhibiting the growth of authigenic
570 quartz (e.g. Heald and Larese, 1974; Ehrenberg, 1993; Bloch et al., 2002; Anjos et al., 2003; Dowey
571 et al., 2012). Authigenic quartz growth is accelerated in basins with higher heat flows (e.g.
572 Walderhaug, 1994), such as the northern Norwegian Sea (e.g. Ritter et al., 2004). In these cases,
573 deposits with higher matrix contents, whilst exhibiting lower initial porosity and permeability, may
574 act to preserve the porosity and permeability present during deeper burial. Consequently, porosity
575 and permeability in architectural element positions with lower matrix contents (e.g. lobe axis) are
576 more likely to be reduced by authigenic quartz growth. A balance of the initial porosity and
577 permeability, and that preserved from authigenic quartz, may favour medial values of grain-size
578 and matrix content in these cases, such as lobe off-axis deposits. However, as temperature and
579 compaction increase with burial the diagenetic overprint control on reservoir quality is likely to
580 become stronger relative to the depositional control (see also: Porten et al., 2016).

581 **8.1 Conclusions**

582 Two deep-water architectural elements, a channel-fill element and a lobe, are characterized
583 at grain-scale using quantitative methodology to map depositional reservoir quality spatially within
584 individual architectural elements for the first time. Quantification of these data and their rates of
585 change can be important parameters for sub-surface predictability and fluid flow simulation
586 models. Textural and architectural properties show strong spatial variation in both elements. The

587 distribution of initial depositional reservoir quality within, and between sub-environments is
588 controlled by flow processes and their spatial and temporal evolution.

589 Within the channel-fill element, channel-axis deposits have the best depositional reservoir
590 quality as they have the coarsest grain-size and lowest matrix content. However, depositional
591 reservoir quality decreases upwards within the channel-axis, as the proportion of high-density
592 turbidites decreases, and low-density turbidites increases as the channel-fill aggrades. Channel-
593 margin deposits consist of low-density turbidites which have low reservoir potential due to their
594 finer grain-sizes and high matrix content. Channel-axis deposits are also more amalgamated, and
595 contain a greater thickness of sandstone, therefore they have better connectivity and volume
596 compared to channel-margin deposits. Lobe axis deposits are dominated by high-density
597 turbidites, which have better depositional reservoir quality compared to the lobe off-axis and lobe
598 fringe as they have the coarsest grain-size, lowest matrix content, most amalgamation and highest
599 net-to-gross. Lobe off-axis deposits contain a mixture of high- and low-density turbidites, giving
600 moderate depositional reservoir quality. Lobe fringe deposits are characterized by low-density
601 turbidites, which have the poorest depositional reservoir quality as they have the finest grain-size,
602 highest matrix content, lowest degree of amalgamation and lowest net-to-gross. The rate of change
603 in grain-size, matrix content and amalgamation increases from lobe off-axis to lobe fringe. This
604 suggests reservoir potential decreases more abruptly from the lobe off-axis into the lobe fringe
605 compared to from the lobe axis to lobe off-axis. However, in basin-fills with high heat-flow, sub-
606 environments with increased detrital matrix and clay-coating of grains which inhibit authigenic
607 quartz growth (e.g. lobe off-axis), may preserve initial porosity and permeability post-diagenesis.
608 The studied deep-water architectural elements exhibit similar meso-scale facies, stacking patterns
609 and lithofacies distributions to deep-water systems of different basins, ages and delivery systems.
610 Quantified depositional reservoir quality distribution intimately ties to this predictable facies
611 organisation and should therefore be predictable elsewhere.

612 **Acknowledgments**

613 The authors are grateful to the AAPG Foundation Grants-In-Aid program for the award of the R. Dana
614 Russell memorial grant, which part-funded this research. We thank Salvatore Critelli for his editorial
615 handling of the paper and the reviews of Salvatore Milli and an anonymous reviewer whose comments
616 enhanced the clarity of the manuscript.

617 **References**

- 618 Aehnelt, M., Worden, R.H., Canham, A.C., Hill, S.J., Hodgson, D.M., and Flint, S.S., 2013,
619 Geochemical correlation in an exhumed submarine channel complex (Tabernas Basin, SE
620 Spain): Comparison to sedimentological correlation at various length scales: *Journal of*
621 *Sedimentary Research*, v. 83, no. 8, p. 669–690, doi: 10.2110/jsr.2013.41.
- 622 Afifi, A.M., 2005, The anatomy of the world's largest oil field: *AAPG Search and Discovery*, v.
623 Article 20.
- 624 Ajdukiewicz, J.M., Nicholson, P.H., and Esch, W.L., 2010, Prediction of deep reservoir quality
625 using early diagenetic process models in the Jurassic Norphlet Formation, Gulf of Mexico:
626 *AAPG Bulletin*, v. 94, no. 8, p. 1189–1227, doi: 10.1306/04211009152.
- 627 Al Ja'aidi, O.S., McCaffrey, W.D., and Kneller, B.C., 2004, Factors influencing the deposit
628 geometry of experimental turbidity currents: implications for sand-body architecture in
629 confined basins, *in* Lomas, S.A. and Joseph, P. eds., *Confined Turbidite Systems*,
630 Geological Society, London, Special Publications, London, p. 45–58.
- 631 Allen, J.R.L., 1982, *Sedimentary structures*, Vol. 1-2: Elsevier, Amsterdam.
- 632 Allen, J.R.L., and Friend, P.F., 1976, Relaxation time of dunes in decelerating aqueous flows:
633 *Journal of the Geological Society*, v. 132, no. 1, p. 17–26.
- 634 Anjos, S.M.C., De Ros, L.F., and Silva, C.M.A., 2003, Chlorite authigenesis and porosity
635 preservation in the Upper Cretaceous marine sandstones of the Santos Basin, offshore

636 eastern Brazil, *in* Worden, R., and Morad, S. eds., Clay Mineral Cements in Sandstones,
637 Special Publication Number 34 of the International Association of Sedimentologists, p.
638 291–316.

639 Baas, J.H., Kesteren, W.V.A.N., and Postma, G., 2004, Deposits of depletive high-density
640 turbidity currents : a flume analogue of bed geometry , structure and texture:
641 Sedimentology, v. 51, p. 1053–1088, doi: 10.1111/j.1365-3091.2004.00660.x.

642 Baas, J.H., Best, J.L., and Peakall, J., 2011, Depositional processes , bedform development and
643 hybrid bed formation in rapidly decelerated cohesive (mud-sand) sediment flows .
644 Sedimentology: Sedimentology, v. 58, no. July 2016, p. 1953–1987, doi: 10.1111/j.1365-
645 3091.2011.01247.x.

646 Barton, M., O’Byrne, C., Pirmez, C., Prather, B., van Der Vlugt, F., Alpak, F.O., and Sylvester,
647 Z., 2010, Turbidite channel architecture: recognizing and quantifying the distribution of
648 channel-base drapes using core and dipmeter data, *in* Pöppelreiter, M., García-Carballido,
649 C., and Kraaijveld, M. eds., Dipmeter and borehole image log technology, AAPG Memoir
650 92, p. 195–210.

651 Bayliss, N.J., and Pickering, K.T., 2015, Deep-marine structurally confined channelised sandy
652 fans: Middle Eocene Morillo System, Ainsa Basin, Spanish Pyrenees: Earth Science
653 Reviews, v. 144, p. 82–106, doi: 10.1016/j.earscirev.2014.11.014.

654 Beard, D.C., and Weyl, P.K., 1973, Influence of texture on porosity of unconsolidated sands:
655 AAPG Bulletin, v. 57, no. 2, p. 349–369, doi: 10.1306/819A4272-16C5-11D7-
656 8645000102C1865D.

657 Beaubouef, R.T., 2004, Deep-water leveed-channel complexes of the Cerro Toro Formation,
658 Upper Cretaceous, southern Chile: AAPG Bulletin, v. 88, no. 11, p. 1471–1500, doi:
659 10.1306/06210403130.

660 Bell, D., Stevenson, C.J., Kane, I.A., Hodgson, D.M., and Poyatos-Moré, M. *in press*, The role of
661 seabed topography in the development of contemporaneous but contrasting depositional
662 architectures in a basin-floor system: *Journal of Sedimentary Research*,

663 Best, J.L., and Bridge, J.S., 1992, The morphology and dynamics of low amplitude bedwaves
664 upon upper stage plane beds and the preservation of planar laminae: *Sedimentology*, v. 39,
665 p. 737–752, doi: 10.1111/j.1365-3091.1992.tb02150.x.

666 Bloch, S., Lander, R.H., and Bonnell, L., 2002, Anomalously high porosity and permeability in
667 deeply buried sandstone reservoirs: Origin and predictability: *AAPG Bulletin*, v. 86, no. 2,
668 p. 301–328, doi: 10.1306/61EEDABC-173E-11D7-8645000102C1865D.

669 Caja, M.A., Marfil, R., Garcia, D., Remacha, E., Morad, S., Mansurbeg, H., Amorosi, A.,
670 Martínez-Calvo, C., and Lahoz-Beltrá, R., 2010, Provenance of siliciclastic and hybrid
671 turbiditic arenites of the Eocene Hecho Group, Spanish Pyrenees: Implications for the
672 tectonic evolution of a foreland basin: *Basin Research*, v. 22, no. 2, p. 157–180, doi:
673 10.1111/j.1365-2117.2009.00405.x.

674 Champion, K.M., Sprague, A.R., Mohrig, D., Lovell, R.W., Drzewiecki, P.A., Sullivan, M.D.,
675 Ardill, J.A., Jensen, G.N., and Sickafoose, D.K., 2000, Outcrop expression of confined
676 channel complexes, *in* Weimar, P., Slatt, R.M., Coleman, J., Rosen, N.C., Nelson, H.,
677 Bouma, A.H., Styzen, M.J., and Lawrence, D.T. eds., *Deep-Water Reservoirs of the World*:
678 SEPM, Gulf Coast Section, 20th Annual Research Conference, p. 127–151.

679 Cartigny, M.J.B., Eggenhuisen, J.T., Hansen, E.W.M., and Postma, G., 2013, Concentration-
680 dependent flow stratification in experimental high-density turbidity currents and their
681 relevance to turbidite facies models: *Journal of Sedimentary Research*, v. 83, p. 1046–1064,
682 doi: 10.2110/jsr.2013.71.

683 Clare, M.A., Talling, P.J., Challenor, P., Malgesini, G., and Hunt, J., 2014, Distal turbidites reveal
684 a common distribution for large (>0.1 km³) submarine landslide recurrence: *Geology*, v. 42,

685 no. 3, p. 263–266.

686 Clark, J.D., Kenyon, N.H., and Pickering, K.T., 1992, Quantitative analysis of the geometry of
687 submarine channels: implications for the classification of submarine fans: *Geology*, v. 20,
688 no. 7, p. 633–636, doi: 10.1130/0091-7613(1992)020<0633:QAOTGO>2.3.CO.

689 Clark, J.D., and Pickering, K.T., 1996, Architectural elements and growth patterns of submarine
690 channels: Application to hydrocarbon exploration: *AAPG Bulletin*, v. 80, p. 194–221, doi:
691 10.1306/64ED878C-1724-11D7-8645000102C1865D.

692 Clark, J.D., Puigdefàbregas, C., Castelltort, S., and Fildani, A., 2017, Propagation of
693 Environmental Signals within Source-to-Sink Stratigraphy: *SEPM Field Trip Guidebook 13*, p.
694 1–63.

695 Dakin, N., Pickering, K.T., Mohrig, D., and Bayliss, N.J., 2013, Channel-like features created by
696 erosive submarine debris flows: Field evidence from the Middle Eocene Ainsa Basin,
697 Spanish Pyrenees: *Marine and Petroleum Geology*, v. 41, p. 62–71, doi:
698 10.1016/j.marpetgeo.2012.07.007.

699 Das Gupta, K., and Pickering, K.T., 2008, Petrography and temporal changes in petrofacies of
700 deep-marine Ainsa – Jaca basin sandstone systems , Early and Middle Eocene , Spanish
701 Pyrenees: *Sedimentology*, v. 55, no. 4, p. 1083–1114, doi: 10.1111/j.1365-
702 3091.2007.00937.x.

703 Deptuck, M.E., Piper, D.J.W., Savoye, B., and Gervais, A., 2008, Dimensions and architecture of
704 late Pleistocene submarine lobes off the northern margin of East Corsica: *Sedimentology*, v.
705 55, p. 869–898.

706 Di Celma, C.N., Brunt, R.L., Hodgson, D.M., Flint, S.S., and Kavanagh, J.P., 2011, Spatial and
707 Temporal Evolution of a Permian Submarine Slope Channel-Levee System, Karoo Basin,
708 South Africa: *Journal of Sedimentary Research*, v. 81, no. 8, p. 579–599, doi:
709 10.2110/jsr.2011.49.

710 Di Celma, C., Teloni, R., and Rustichelli, A., 2014, Large-scale stratigraphic architecture and
711 sequence analysis of an early Pleistocene submarine canyon fill , Monte Ascensione
712 succession (Peri-Adriatic basin, eastern central Italy): *International Journal of Earth*
713 *Sciences*, v. 103, no. 3, p. 843–875, doi: 10.1007/s00531-013-0984-3.

714 Dickinson, W.R., 1970, Interpreting detrital modes of graywacke and arkose: *Journal of*
715 *Sedimentary Research*, v. 40, no. 2, p. 695 LP-707.

716 Dowey, P.J., Hodgson, D.M., and Worden, R.H., 2012, Pre-requisites, processes, and prediction
717 of chlorite grain coatings in petroleum reservoirs: A review of subsurface examples: *Marine*
718 *and Petroleum Geology*, v. 32, no. 1, p. 63–75, doi: 10.1016/j.marpetgeo.2011.11.007.

719 Ehrenberg, S.N., 1989, Assessing the relative importance of compaction processes: *AAPG*
720 *Bulletin*, v. 73, no. 10, p. 1274–1276.

721 Ehrenberg, S.N., 1993, Preservation of Anomalously High Porosity in Deeply Buried Sandstones
722 by Grain-Coating Chlorite: Examples from the Norwegian Continental Shelf: *AAPG*
723 *Bulletin*, v. 77, no. 7, p. 1260–1286.

724 Ehrenberg, S.N., 1997, Influence of depositional sand quality and diagenesis on porosity and
725 permeability: Examples from Brent Group reservoirs, Northern North Sea: *SEPM Journal*
726 *of Sedimentary Research*, v. 67, no. 1, p. 197–211, doi: 10.1306/D4268531-2B26-11D7-
727 8648000102C1865D.

728 Emmel, F.J., and Curray, J.R., 1983, The Bengal Submarine Fan, Northeastern Indian ocean:
729 *Geo-Marine Letters*, v. 3, no. 2, p. 119–124, doi: 10.1007/BF02462456.

730 Eschard, R., Albouy, E., Deschamps, R., Euzen, T., and Ayub, A., 2003, Downstream evolution
731 of turbiditic channel complexes in the Pab Range outcrops (Maastrichtian, Pakistan):
732 *Marine and Petroleum Geology*, v. 20, no. 6–8, p. 691–710, doi:
733 10.1016/j.marpetgeo.2003.02.004.

734 Fildani, A., Clark, J., Covault, J.A., Power, B., Romans, B.W., and Aiello, I.W., 2018, Muddy sand
735 and sandy mud on the distal Mississippi fan: Implications for lobe depositional processes:
736 *Geosphere*, v. 14, no. 3, p. 1051–1066.

737 Folk, R.L., and Ward, W.C., 1957, Brazos River Bar: A Study in the Significance of Grain Size
738 Parameters: *Journal of Sedimentary Petrology*, v. 27, no. 1, p. 3–26.

739 Fontana, D., Zuffa, G.G., and Garzanti, E., 1989, The interaction of eustacy and tectonism from
740 provenance studies of the Eocene Hecho Group Turbidite Complex (South-Central
741 Pyrenees, Spain): *Basin Research*, v. 2, no. 4, p. 223–237.

742 Fraser, H.J., 1935, Experimental Study of the Porosity and Permeability of Clastic Sediments:
743 *The Journal of Geology*, v. 43, no. 8, p. 910–1010, doi: 10.1086/624388.

744 Galy, V., France-Lanord, C., Beyssac, O., Faure, P., Kudrass, H., and Palhol, F., 2007, Efficient
745 organic carbon burial in the Bengal fan sustained by the Himalayan erosional system:
746 *Nature*, v. 450, p. 407.

747 Garcia, M., 1994, Depositional turbidity currents laden with poorly sorted sediment: *Journal of*
748 *Hydraulic Engineering*, v. 120, no. 11, p. 1240–1263.

749 Gardner, M.H., and Borer, J.M., 2000, Submarine channel architecture along a slope to basin
750 profile, Brushy Canyon Formation, West Texas, *in* Bouma, A.H. and Stone, C.G. eds., *Fine-*
751 *Grained Turbidite Systems: AAPG Memoir 72 and SEPM Special Publication 68*, p. 195–
752 214.

753 Gazzi, P., 1966, Le Arenarie del flysch sopracretaceo dell'Appennino modenese; correlazioni con
754 il flysch di Monghidoro: *Mineralogica e Petrografica Acta*, v. 16, p. 69–97.

755 Gladstone, C., Phillips, J.C., and Sparks, R.S.J., 1998, Experiments on bidisperse, constant
756 volume gravity currents: propagation and sediment deposition: *Sedimentology*, v. 45, p.
757 833–843.

758 Grundvåg, S.A., Johannessen, E.P., Helland-Hansen, W., and Plink-Björklund, P., 2014,
759 Depositional architecture and evolution of progradationally stacked lobe complexes in the
760 Eocene Central Basin of Spitsbergen: *Sedimentology*, v. 61, no. 2, p. 535–569, doi:
761 10.1111/sed.12067.

762 Gwiazda, R., Paull, C.K., Ussler, W., and Alexander, C.R., 2015, Evidence of modern fine-
763 grained sediment accumulation in the Monterey Fan from measurements of the pesticide
764 DDT and its metabolites: *Marine Geology*, v. 363, p. 125–133, doi:
765 <https://doi.org/10.1016/j.margeo.2015.02.006>.

766 Haile, B.G., Klausen, T.G., Czarniecka, U., Xi, K., Jahren, J., and Hellevang, H., 2017, How are
767 diagenesis and reservoir quality linked to depositional facies? A deltaic succession, Edgeøya,
768 Svalbard: *Marine and Petroleum Geology*, v. 92, 519-546 doi:
769 <https://doi.org/10.1016/j.marpetgeo.2017.11.019>.

770 Hardage, B.A., Carr, D.L., Lancaster, D.E., Simmons, J.L., Elphick, R.Y., Pendleton, V.M., and
771 Johns, R.A., 1996, 3-D seismic evidence of the effects of carbonate karst collapse on
772 overlying clastic stratigraphy and reservoir compartmentalization: *Geophysics*, v. 61, no. 5,
773 p. 1336–1350, doi: 10.1190/1.1444057.

774 Heald, M.T., and Larese, R.E., 1974, Influence of coatings on quartz cementation: *Journal of*
775 *Sedimentary Research*, v. 44, no. 4.

776 Hirst, J.P.P., Benbakir, A., Payne, D.F., and Westlake, I.R., 2002, Tunnel valleys and density flow
777 processes in the Upper Ordovician glacial succession, Illizi Basin, Algeria: Influence on
778 reservoir quality: *Journal of Petroleum Geology*, v. 25, no. 3, p. 297–324, doi:
779 10.1111/j.1747-5457.2002.tb00011.x.

780 Hiscott, R.N., Hall, F.R., and Pirmez, C., 1997, Turbidity-current overspill from the Amazon
781 channel: texture of the silt/sand load, paleoflow from anisotropy of magnetic susceptibility
782 and implications for flow processes, *in* Flood, R.D., Piper, D.J.W., Klaus, A., and Peterson,

783 L.C. eds., Proceedings of the Ocean Drilling Program, Scientific Results, Ocean Drilling
784 Program, College Station, Texas, p. 53–78.

785 Hodgson, D.M., 2009, Distribution and origin of hybrid beds in sand-rich submarine fans of the
786 Tanqua depocentre, Karoo Basin, South Africa: *Marine and Petroleum Geology*, v. 26, no.
787 10, p. 1940–1956, doi: 10.1016/j.marpetgeo.2009.02.011.

788 Hodgson, D. M., Kane, I. A., Flint, S. S., Brunt, R. L., & Ortiz-Karpf, A. (2016). Time-
789 transgressive confinement on the slope and the progradation of basin-floor fans:
790 Implications for the sequence stratigraphy of deep-water deposits. *Journal of Sedimentary*
791 *Research*, 86, no. 1, 73-86, doi: 10.2110/jsr.2016.3

792 Hodson, J.M., and Alexander, J., 2010, The Effects of Grain-Density Variation on Turbidity
793 Currents and Some Implications for the Deposition of Carbonate Turbidites: *Journal of*
794 *Sedimentary Research*, v. 80, no. 6, p. 515–528, doi: 10.2110/jsr.2010.051.

795 Hubbard, S.M., Covault, J.A., Fildani, A., and Romans, B.W., 2014, Sediment transfer and
796 deposition in slope channels: Deciphering the record of enigmatic deep-sea processes from
797 outcrop: *Bulletin of the Geological Society of America*, v. 126, no. 5–6, p. 857–871, doi:
798 10.1130/B30996.1.

799 Ingersoll, R. V, Bullard, T.F., Ford, R.L., Grimm, J.P., Pickle, J.D., and Sares, S.W., 1984, The
800 effect of grain size on detrital modes: a test of the Gazzi-Dickinson point-counting method:
801 *Journal of Sedimentary Research*, v. 54, no. 1, p. 103–116.

802 Jolley, S.J., Fisher, Q.J., and Ainsworth, R.B., 2010, Reservoir compartmentalization: an
803 introduction: Geological Society, London, Special Publications, v. 347, no. 1, p. 1 LP-8.

804 Kane, I.A., and Pontén, A.S.M., 2012, Submarine transitional flow deposits in the Paleogene
805 Gulf of Mexico: *Geology*, v. 40, no. 12, p. 1119–1122, doi: 10.1130/G33410.1.

806 Kane, I.A., Pontén, A.S.M., Vangdal, B., Eggenhuisen, J.T., Hodgson, D.M., and Spychala, Y.T.,

807 2017, The stratigraphic record and processes of turbidity current transformation across
808 deep-marine lobes: *Sedimentology*, doi: 10.1111/SED.12346.

809 Kerr, D.R., and Jirik, L.A., 1990, Fluvial architecture and reservoir compartmentalization in the
810 Oligocene Middle Frio Formation of South Texas: *AAPG Bulletin*, v. 74, p. 373–380, doi:
811 10.1306/20B2311F-170D-11D7-8645000102C1865D.

812 Kilhams, B., Hartley, A., Huuse, M., and Davis, C., 2015, Characterizing the Paleocene turbidites
813 of the North Sea : Maureen Formation, UK Central Graben, *in* Mckie, T., Rose, P.T.S.,
814 Hartley, A., Jones, D.W., and Armstrong, T.L. eds., *Tertiary Deep-Marine Reservoirs of the*
815 *North Sea Reservoirs of the North Sea Region*, Geological Society, London, p. 43–62.

816 Kilhams, B., Hartley, A., Huuse, M., and Davis, C., 2012, Characterizing the Paleocene turbidites
817 of the North Sea: the Mey Sandstone Member, Lista Formation, UK Central Graben:
818 *Petroleum Geoscience*, v. 18, p. 337–354, doi: 10.1144/SP403.1.

819 Labaume, P., Mutti, E., and Seguret, M., 1987, Megaturbidites : A Depositional Model From the
820 Eocene: *Geo-Marine Letters*, v. 7, no. 2, p. 91–101.

821 Labaume, P., Séguret, M., and Seyve, C., 1985, Evolution of a turbiditic foreland basin and
822 analogy with an accretionary prism: Example of the Eocene South-Pyrenean Basin:
823 *Tectonics*, v. 4, no. 7, p. 661, doi: 10.1029/TC004i007p00661.

824 Lan, C., Yang, M., and Zhang, Y., 2016, Impact of sequence stratigraphy, depositional facies and
825 diagenesis on reservoir quality: A case study on the Pennsylvanian Taiyuan sandstones,
826 northeastern Ordos Basin, China: *Marine and Petroleum Geology*, v. 69, p. 216–230, doi:
827 10.1016/j.marpetgeo.2015.09.009.

828 Li, P., Kneller, B.C., Hansen, L., and Kane, I.A., 2016, The classical turbidite outcrop at San
829 Clemente, California revisited: An example of sandy submarine channels with asymmetric
830 facies architecture: *Sedimentary Geology*, v. 346, p. 1–16, doi:

831 10.1016/j.sedgeo.2016.10.001.

832 Lien, T., Midtbø, R.E., and Martinsen, O.J., 2006, Depositional facies and reservoir quality of
833 deep-marine sandstones in the Norwegian Sea: *Norwegian Journal of Geology*, v. 86, no. 2,
834 p. 71–92

835 Lowe, D.R., 1982, Sediment Gravity Flows: II Depositional Models with Special Reference to
836 the Deposits of High-Density Turbidity Currents: *Journal of Sedimentary Research*, v. 52,
837 no. 1.

838 Marchand, A.M.E., Apps, G., Li, W., and Rotzien, J.R., 2015, Depositional processes and impact
839 on reservoir quality in deepwater Paleogene reservoirs, US Gulf of Mexico: *AAPG Bulletin*,
840 v. 99, no. 9, p. 1635–1648, doi: 10.1306/04091514189.

841 Marini, M., Milli, S., Ravnås, R., and Moscatelli, M., 2015, A comparative study of confined vs.
842 semi-confined turbidite lobes from the Lower Messinian Laga Basin (Central Apennines,
843 Italy): implications for assesment of reservoir architecture: *Marine and Petroleum Geology*,
844 v. 63, p. 142–165, doi: 10.1016/j.marpetgeo.2015.02.015.

845 Marzano, M.S., 1988, Controls on permeability for unconsolidated sands from conventional core
846 data offshore Gulf of Mexico: *AAPG bulletin*, v. 38, p. 113–120.

847 McHargue, T., Pyrcz, M.J., Sullivan, M.D., Clark, J.D., Fildani, A., Romans, B.W., Covault, J.A.,
848 Levy, M., Posamentier, H.W., and Drinkwater, N.J., 2011, Architecture of turbidite channel
849 systems on the continental slope: Patterns and predictions: *Marine and Petroleum Geology*,
850 v. 28, no. 3, p. 728–743, doi: 10.1016/j.marpetgeo.2010.07.008.

851 McKie, T., Rose, P.T.S., Hartley, A.J., Jones, D.W., and Armstrong, T.L., 2015, Tertiary deep-
852 marine reservoirs of the North Sea region: an introduction, *in* McKie, T., Rose, P.T.S.,
853 Hartley, A.J., Jones, D.W., and Armstrong, T.L. eds., *Tertiary Deep-Marine Reservoirs of*
854 *the North Sea Reservoirs of the North Sea*, The Geological Society of London, p. 403.

855 Miall, A.D., 1985, Architectural-Element Analysis: A New Method of Facies Analysis Applied to
856 Fluvial Deposits: *Earth-Science Reviews*, v. 22, no. 4, p. 261–308.

857 Middleton, G. V., 1967, Experiments on density and turbidity currents: III. Deposition of
858 sediment: *Canadian Journal of Earth Sciences*, v. 4, no. 3, p. 475–505, doi: 10.1139/e67-
859 025.

860 Moody, J.D., Pyles, D.R., Clark, J., and Bouroullec, R., 2012, Quantitative outcrop
861 characterization of an analog to weakly confined submarine channel systems: Morillo 1
862 member, Ainsa Basin, Spain: *AAPG Bulletin*, v. 96, no. 10, p. 1813–1841, doi:
863 10.1306/01061211072.

864 Muñoz, J.A., 1992, Evolution of a continental collision belt: ECORS-Pyrenees crustal balanced
865 cross-section, *in* McClay, K.R. ed., *Thrust Tectonics*, Springer Netherlands, Dordrecht, p.
866 235–246.

867 Mutti, E., 1977, Distinctive thin-bedded turbidite facies and related depositional environments in
868 the Eocene Hecho Group (South-central Pyrenees, Spain): *Sedimentology*, v. 24, no. 1, p.
869 107–131, doi: 10.1111/j.1365-3091.1977.tb00122.x.

870 Mutti, E., 1984, The Hecho Eocene submarine fan system, south-central Pyrenees, Spain: *Geo-*
871 *Marine Letters*, v. 3, no. 2–4, p. 199–202, doi: 10.1007/BF02462468.

872 Mutti, E., 1985, Turbidite Systems and Their Relations to Depositional Sequences, *in* Zuffa,
873 G.G. ed., *Provenance of Arenites*, Reidel Publishing Co., Dordrecht, p. 65–93.

874 Mutti, E., 1992, *Turbidite Sandstones*: Agip, Istituto di Geologia Università di Parma, Milan.

875 Mutti, E., and Ricci-Lucchi, F., 1972, Le torbiditi dell'Appennino settentrionale: introduzioni
876 all'analisi di facies: *Mem. Soc. Geol. Ital.*, v. 11/2, p. 161–199, doi: -.

877 Mutti, E., and Normark, W.R., 1987, Comparing Examples of Modern and Ancient Turbidite
878 Systems: Problems and Concepts, *in* Leggett, J.K. and Zuffa, G.G. eds., *Marine clastic*

879 sedimentology, Springer Netherlands, Dordrecht, p. 1–38.

880 Mutti, E., Séguret, M., and Sgavetti, M., 1988, Sedimentation and deformation in the Tertiary
881 Sequences of the Southern Pyrenees: Field trip 7: University of Parma.

882 Nardin, T.R., Hein, F.J., Gorsline, D.S., and Edwards, B., 1979, A Review of mass movement
883 processes, sediment and acoustic characteristics, and contrasts in slope and base-of-slope
884 systems versus canyon-fan-basin floor systems: SEPM Special Publications, , no. 27, p. 61–
885 73.

886 Njoku, C., and Pirmez, C., 2011, Sedimentary Controls on Porosity and Permeability in
887 Deepwater Turbidites: Nigeria Annual International Conference and Exhibition, p. 1–5,
888 doi: 10.2118/150805-ms.

889 Payros, A., Pujalte, V., and Orue-Etxebarria, X., 1999, The South Pyrenean Eocene carbonate
890 megabreccias revisited: New interpretation based on evidence from the Pamplona Basin:
891 Sedimentary Geology, v. 125, no. 3, p. 165–194, doi: 10.1016/S0037-0738(99)00004-4.

892 Pettijohn, F.J., Potter, P.E., and Siever, R., 1972, Sand and Sandstone: Springer, Berlin-
893 Herdelberg-New York. p. 1-553

894 Pettingill, H.S., 1998, Turbidite plays' immaturity means big potential remains: Oil & Gas
895 Journal, v. 96, no. 40, p. 106–111

896 Pickering, K.T., and Corregidor, J., 2005, Mass-transport complexes, (MTCs) and tectonic
897 control on basin-floor submarine fans, middle eocene, south Spanish Pyrenees: Journal of
898 Sedimentary Research, v. 75, no. 5, p. 761–783, doi: 10.2110/jsr.2005.062.

899 Piper, D., Cochonat, P., and Morrison, M.L., 1999, The sequence of events around the epicentre
900 of the 1929 Grand Banks earthquake: Initiation of debris flows and turbidity current
901 inferred from sidescan sonar: Sedimentology, v. 46, p. 79–97, doi: 10.1046/j.1365-
902 3091.1999.00204.x.

- 903 Pittman, E.D., and Larese, R.E., 1991, Compaction of Lithic Sands: Experimental Results and
904 Applications (1): AAPG Bulletin, v. 75, no. 8, p. 1279–1299.
- 905 Porten, K.W., Kane, I.A., Warchol, M., and Southern, S.J., 2016, Depositional reservoir quality
906 of deep-marine sandstones: A sedimentological process-based approach - an example from
907 the Springrar Formation, North-Western Vøring Basin, Norwegian Sea: Journal of
908 Sedimentary Research, v. 86, no. 11, p. 1269–1286.
- 909 Prélat, A., Hodgson, D.M., and Flint, S.S., 2009, Evolution, architecture and hierarchy of
910 distributary deep-water deposits: a high-resolution outcrop investigation from the Permian
911 Karoo Basin, South Africa: Sedimentology, v. 56, no. 7, p. 2132–2154, doi: 10.1111/j.1365-
912 3091.2009.01073.x.
- 913 Prélat, A., Covault, J.A., Hodgson, D.M., Fildani, A., and Flint, S.S., 2010, Intrinsic controls on
914 the range of volumes, morphologies, and dimensions of submarine lobes: Sedimentary
915 Geology, v. 232, no. 1, p. 66–76, doi: 10.1016/j.sedgeo.2010.09.010.
- 916 Pryor, W.A., 1973, Permeability-porosity patterns and variations in some Holocene sand bodies:
917 AAPG Bulletin, v. 57, no. 1, p. 162–189, doi: 10.1306/819A4252-16C5-11D7-
918 8645000102C1865D.
- 919 Puigdefàbregas, C., Rupke, N.A., and Sedo, J.S., 1975, The sedimentary evolution of the Jaca
920 Basin, *in* The Sedimentary Evolution of the Palaeogene South Pyrenean Basin.
- 921 Pyles, D.R., Straub, K.M., and Stammer, J.G., 2013, Spatial variations in the composition of
922 turbidites due to hydrodynamic fractionation: Geophysical Research Letters, v. 40, no.
923 August 2013, p. 3919–3923, doi: 10.1002/grl.50767.
- 924 Ramm, M., and Bjørlykke, K., 1994, Porosity/depth trends in reservoir sandstones: Assessing the
925 quantitative effects of varying pore-pressure, temperature history and mineralogy,
926 Norwegian Shelf data: Clay Minerals, v. 29, p. 475–490.

- 927 Remacha, E., and Fernández, L.P., 2003, High-resolution correlation patterns in the turbidite
928 systems of the Hecho Group (South-Central Pyrenees, Spain): *Marine and Petroleum*
929 *Geology*, v. 20, no. 6, p. 711–726, doi: 10.1016/j.marpetgeo.2003.09.003.
- 930 Remacha, E., Gual, G., Bolaño, F., Arcuri, M., Oms, O., Climent, F., Crumeyrolle, P.,
931 Fernández, L.P., Vicente, J.C., and Suarez, J., 2003, Sand-rich turbidite systems of the
932 Hecho Group from slope to basin plain; facies, stacking patterns, controlling factors and
933 diagnostic features: American Association of Petroleum Geologists, International
934 Conference and Exhibition, Barcelona, Spain, September 21–24. *Geological field trip 12, South-*
935 *Central Pyrenees*.
- 936 Remacha, E., Fernández, L.P., and Maestro, E., 2005, The Transition Between sheet-like lobe
937 and basin-plain turbidites in the Hecho Basin (South-Central Pyrenees, Spain): *Journal of*
938 *Sedimentary Research*, v. 75, no. 5, p. 798–819, doi: 10.2110/jsr.2005.064.
- 939 Ritter, U., Zielinski, G.W., Weiss, H.M., Zielinski, R.L.B., and Sættem, J., 2004, Heat flow in the
940 Vøring Basin, Mid-Norwegian Shelf: *Petroleum Geoscience*, v. 10, no. 4, p. 353–365, doi:
941 <https://doi.org/10.1144/1354-079303-616>.
- 942 Rosell, J., and Wiczorek, J., 1989, Main features of megaturbidites in the Eocene of southern
943 Pyrenees: *Annales Societatis Geologorum Poloniae*, v. 59, p. 3–16.
- 944 Ruffell, A.H., Moles, N.R., and Parnell, J., 1998, Characterisation and prediction of sediment-
945 hosted ore deposits using sequence stratigraphy: *Ore Geology Reviews*, v. 12, no. 4, p. 207–
946 223, doi: [https://doi.org/10.1016/S0169-1368\(97\)00029-2](https://doi.org/10.1016/S0169-1368(97)00029-2).
- 947 Rupke, N.A., 1976, Sedimentology of very thick calcarenite-marlstone beds in a flysch
948 succession, southwestern Pyrenees: *Sedimentology*, v. 23, p. 213–265, doi: 10.1111/j.1365-
949 3091.1976.tb00038.x.
- 950 Saller, A., Werner, K., Sugiaman, F., Cebastian, A., May, R., Glenn, D., and Barker, C., 2008,
951 Characteristics of Pleistocene deep-water fan lobes and their application to an upper

952 Miocene reservoir model, offshore East Kalimantan, Indonesia: AAPG Bulletin, v. 92, no.
953 7, p. 919–949, doi: 10.1306/03310807110.

954 Sanders, J.E., 1965, Primary sedimentary structures formed by turbidity currents and related
955 resuspension mechanisms, *in* Middleton, G.V. ed., Primary Sedimentary Structures and their
956 Hydrodynamic Interpretation, SEPM Special Publication, p. 192–219.

957 Southard, J.B., 1991, Experimental Determination of Bed-Form Stability: Annual Review of
958 Earth and Planetary Sciences, v. 19, no. 1, p. 423–455, doi:
959 10.1146/annurev.ea.19.050191.002231.

960 Southern, S.J., Kane, I.A., Warchol, M.J., Porten, K.W., and McCaffrey, W.D., 2017, Hybrid
961 event beds dominated by transitional-flow facies: Character, distribution and significance in
962 the maastrichtian springar formation, north-west vøring basin, Norwegian Sea:
963 Sedimentology, v. 64, no. 3, p. 747–776, doi: 10.1111/sed.12323.

964 Sprague, A.R., Sullivan, M.D., Campion, K.M., Jensen, G.N., Goulding, F.J., Garfield, T.R.,
965 Sickafoose, D.K., Rossen, C., and Jeannette, D.C., 2002, The physical stratigraphy of deep-
966 water strata: A hierarchical approach to the analysis of genetically-related stratigraphic
967 elements for improved reservoir prediction, *in* National AAPG/SEPM meeting abstracts,
968 Houston, Texas, p. 10–13.

969 Spychala, Y.T., Hodgson, D.M., Prélat, A., Kane, I.A., Flint, S.S., and Mountney, N.P., 2017a,
970 Frontal and lateral submarine lobe fringes: Comparing facies, architecture and flow
971 processes: Journal of Sedimentary Research, v. 87, no. January, p. 1–21.

972 Spychala, Y.T., Hodgson, D.M., and Stevenson, C.J., 2017b, Aggradational lobe fringes : The
973 influence of subtle intrabasinal seabed topography on sediment gravity flow processes and
974 lobe stacking patterns: Sedimentology, v. 64, p. 582–608, doi: 10.1111/sed.12315.

975 Stalder, N.F., Fellin, M.G., Caracciolo, L., Guillong, M., Winkler, W., Milli, S., Moscatelli, M., and
976 Critelli, S., 2017, Dispersal pathways in the early Messinian Adriatic foreland and

977 provenance of the Laga Formation (Central Apennines, Italy): *Sedimentary Geology*, doi:
978 <https://doi.org/10.1016/j.sedgeo.2017.09.016>.

979 Stevenson, C.J., Talling, P.J., Masson, D.G., Sumner, E.J., Frenz, M., and Wynn, R.B., 2014a,
980 The spatial and temporal distribution of grain-size breaks in turbidites: *Sedimentology*, v.
981 61, p. 1120–1156, doi: 10.1111/sed.12091.

982 Stevenson, C.J., Talling, P.J., Sumner, E.J., Masson, D.G., Frenz, M., and Wynn, R., 2014b, On
983 how thin submarine flows transported large volumes of sand for hundreds of kilometres
984 across a flat basin plain without eroding the sea floor: *Sedimentology*, p. n/a-n/a, doi:
985 10.1111/sed.12125.

986 Stevenson, C.J., Jackson, C.A.-L., Hodgson, D.M., Hubbard, S.M., and Eggenhuisen, J.T., 2015,
987 Deep-water sediment bypass: *Journal of Sedimentary Research*, v. 85, p. 1058–1081, doi:
988 10.2110/jsr.2015.63.

989 Sullivan, M.D., Jensen, G.N., Goulding, F.J., Jennette, D.C., Foreman, J.L., and Stern, D., 2000,
990 Architectural analysis of deep-water outcrops: Implications for exploration and
991 development of the Diana sub-basin, western Gulf of Mexico, *in* Weimer, P., Slatt, R.M.,
992 Bouma, A.H., and Lawrence, D.T. eds., *Deep-water reservoirs of the world*, Gulf Coast
993 Section SEPM Foundation, Twentieth Annual Research Conference, p. 1010–1032.

994 Sumner, E.J., Amy, L.A., and Talling, P.J., 2008, Deposit Structure and Processes of Sand
995 Deposition from Decelerating Sediment Suspensions: *Journal of Sedimentary Research*, v.
996 78, no. 8, p. 529–547, doi: 10.2110/jsr.2008.062.

997 Sumner, E.J., Talling, P.J., Amy, L.A., Wynn, R.B., Stevenson, C.J., and Frenz, M., 2012, Facies
998 architecture of individual basin-plain turbidites: Comparison with existing models and
999 implications for flow processes: *Sedimentology*, v. 59, p. 1850–1887, doi: 10.1111/j.1365-
1000 3091.2012.01329.x.

1001 Talling, P.J., Wynn, R.B., Masson, D.G., Frenz, M., Cronin, B.T., Schiebel, R., Akhmetzhanov,

1002 A.M., Dallmeier-Tiessen, S., Benetti, S., Weaver, P.P.E., Georgiopoulou, A., Zühlendorff, C.,
1003 and Amy, L.A., 2007, Onset of submarine debris flow deposition far from original giant
1004 landslide.: *Nature*, v. 450, no. November, p. 541–544, doi: 10.1038/nature06313.

1005 Talling, P.J., Masson, D.G., Sumner, E.J., and Malgesini, G., 2012, Subaqueous sediment density
1006 flows: Depositional processes and deposit types: *Sedimentology*, v. 59, p. 1937–2003, doi:
1007 10.1111/j.1365-3091.2012.01353.x.

1008 Teixell, A., and García-Sansegundo, J., 1995, Estructura del sector central de la Cuenca de Jaca
1009 (Pirineos meridionales): *Rev. Soc. Geol. España*, v. 8, no. 3, p. 215–228.

1010 Walderhaug, O., 1994, Precipitation rates for quartz cement in sandstones determined by fluid-
1011 inclusion microthermometry and temperature-history modeling: *Journal of Sedimentary*
1012 *Research*, v. A64, no. 2, p. 324–333.

1013 Walker, R.G., 1975, Generalized facies models for resedimented conglomerates of turbidite
1014 association: *Geological Society of America Bulletin*, v. 86, no. 6, p. 737–748.

1015 Weimer, P., Slatt, R.M., Dromgoole, P., Bowman, M., and Leonard, A., 2000, Developing and
1016 Managing Turbidite Reservoirs : Case Histories and Experiences : Results of the 1998
1017 EAGE/AAPG Research Conference 1: *AAPG Bulletin*, v. 84, no. 4, p. 453–465.

1018 Wilson, M.D., 1992, Inherited grain-rimming clays in sandstones from eolian and shelf
1019 environments: their origin and control on reservoir properties, *in* *Origin Diagenesis and*
1020 *Petrophysics of Clay Minerals in Sandstones*, SEPM Special Publication No. 47, p. 209–225.

1021 Worden, R.H., Mayall, M., and Evans, I.J., 2000, The Effect of Ductile-Lithic Sand Grains and
1022 Quartz Cement on Porosity and Permeability in Oligocene and Lower Miocene Clastics ,
1023 South China Sea : Prediction of Reservoir Quality 1: *AAPG Bulletin*, v. 84, no. 3, p. 345–
1024 359.

1025 Zuffa, G.G., Cibin, U., and Di Giulio, A., 1995, Arenite petrography in sequence stratigraphy:

1026 The Journal of Geology, v. 103, no. 4, p. 451–459.

1027